Cell Reports

Multiple Molecular Mechanisms Rescue mtDNA Disease in *C. elegans*

Graphical Abstract

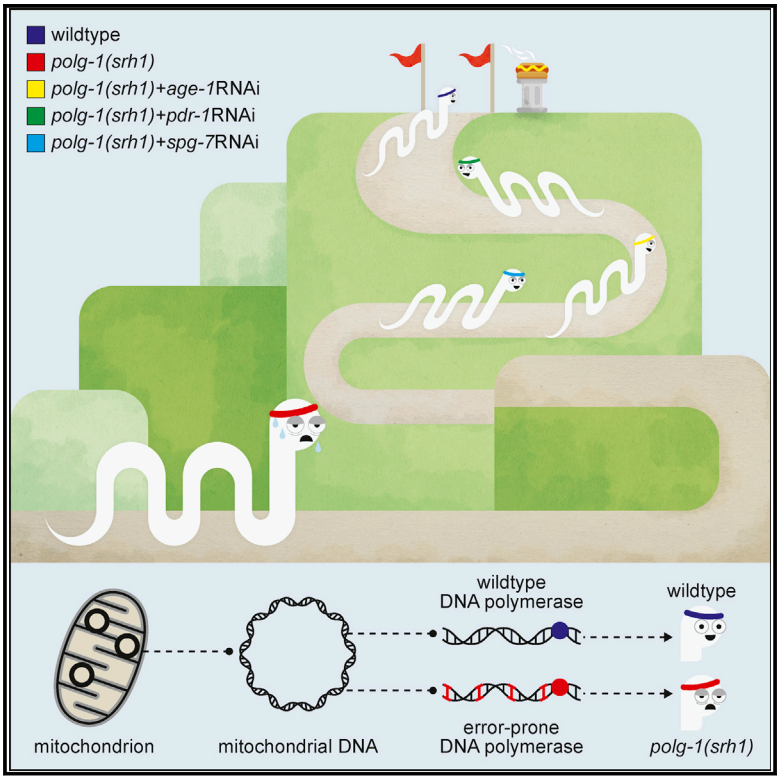

Highlights

- A genetically engineered worm recapitulates the hallmarks of mtDNA disease in humans
- This worm can be exploited to generate countless additional models of mtDNA disease
- An RNAi screen identifies 25 genes that can prevent or delay mtDNA disease in worms
- IGF-1/insulin signaling, mitophagy, and UPR^{mt} strongly affect disease progression

Authors

Suraiya Haroon, Annie Li, Jaye L. Weinert, ..., Jason H. Bielas, Tali Gidalevitz, Marc Vermulst

Correspondence

vermulstm@email.chop.edu

In Brief

Haroon et al. describe a genetically engineered *C. elegans* that carries an error-prone copy of DNA polymerase γ, the enzyme that replicates the mitochondrial genome. This worm recapitulates the major hallmarks of mitochondrial disease in humans. The authors identify multiple biological pathways that could potentially delay disease progression.

Haroon et al., 2018, Cell Reports *22*, 3115–3125
March 20, 2018
https://doi.org/10.1016/j.celrep.2018.02.099

CellPress

Cell Reports
Report

OPEN ACCESS
CellPress

Multiple Molecular Mechanisms Rescue mtDNA Disease in *C. elegans*

Suraiya Haroon,[1] Annie Li,[1] Jaye L. Weinert,[1] Clark Fritsch,[1] Nolan G. Ericson,[2] Jasmine Alexander-Floyd,[3] Bart P. Braeckman,[4] Cole M. Haynes,[5] Jason H. Bielas,[2] Tali Gidalevitz,[3] and Marc Vermulst[1,6,*]
[1]Department of Pathology and Laboratory Medicine, Children's Hospital of Philadelphia, PA 19104, USA
[2]Fred Hutchinson Cancer Research Center, Seattle, WA 98109, USA
[3]Department of Biology, Drexel University, Philadelphia, PA 19104, USA
[4]Laboratory of Aging Physiology and Molecular Evolution, Biology Department, Ghent University, 9000 Ghent, Belgium
[5]Department of Molecular, Cell, and Cancer Biology, University of Massachusetts Medical School, Worcester, MA 01605, USA
[6]Lead Contact
*Correspondence: vermulstm@email.chop.edu
https://doi.org/10.1016/j.celrep.2018.02.099

SUMMARY

Genetic instability of the mitochondrial genome (mtDNA) plays an important role in human aging and disease. Thus far, it has proven difficult to develop successful treatment strategies for diseases that are caused by mtDNA instability. To address this issue, we developed a model of mtDNA disease in the nematode *C. elegans*, an animal model that can rapidly be screened for genes and biological pathways that reduce mitochondrial pathology. These worms recapitulate all the major hallmarks of mtDNA disease in humans, including increased mtDNA instability, loss of respiration, reduced neuromuscular function, and a shortened lifespan. We found that these phenotypes could be rescued by intervening in numerous biological pathways, including IGF-1/insulin signaling, mitophagy, and the mitochondrial unfolded protein response, suggesting that it may be possible to ameliorate mtDNA disease through multiple molecular mechanisms.

INTRODUCTION

Energy animates life. Whether it's protein synthesis, autophagy, or signal transduction, almost every biological process is driven by the consumption of energy. Most of this energy is generated by mitochondria, small tubular organelles that are frequently called the powerhouses of our cells. To optimize energy production, mitochondria carry their own genome called "mtDNA," a small, circular molecule that encodes numerous protein products that are essential to ATP synthesis (Anderson et al., 1981). As a result, loss or mutation of mtDNA invariably affects energy production, which is particularly harmful to cells with high energy demands such as neurons and muscle fibers (Wallace, 2005). Most diseases caused by mtDNA instability are therefore characterized by some form of neuromuscular dysfunction. For example, point mutations, deletions, or overt loss of mtDNA molecules can result in premature deafness, myopathy, or severe encephalomyopathy in children (Saneto and Sedensky, 2013) and contributes to neurodegeneration (Kraytsberg et al., 2006) and muscle wasting (Wanagat et al., 2001) in aging adults. In most cases, mtDNA instability arises spontaneously, although it also can be caused by mutations in DNA polymerase γ, the enzyme that replicates the mitochondrial genome. Thus, the impact of mtDNA instability on human aging and disease is well documented. To this day though, no child has ever been cured of an mtDNA disease, nor does a treatment exist for the mtDNA component of age-related diseases. Although it is now possible to manage the symptoms of a number of pediatric mtDNA diseases, two bottlenecks have traditionally kept the scientific community from developing a more robust treatment strategy: a shortage of animal models and a lack of promising molecules to target. Here, we address these issues by establishing a model of mtDNA disease in worms that can give rise to countless additional models with the proper breeding scheme. Moreover, because worms can be easily manipulated by genetic and pharmaceutical means, we were able to use RNAi, drugs, and genetic mutants to identify multiple cellular pathways that can ameliorate the pathological consequences of mtDNA instability on organismal health, thus providing potential targets for therapeutic intervention. Together, these results suggest that multiple pathways may have evolved to prevent mtDNA disease, underlining the central role that energy plays in cellular life.

RESULTS

A Model of mtDNA Disease in *C. elegans*

To successfully design a therapeutic strategy for mtDNA disease, it will be essential to identify cellular mechanisms that can either increase or decrease the pathology that is caused by mtDNA instability. These experiments will reveal promising targets that can be exploited for therapeutic intervention, and may provide valuable insight into the basic biology that underlies mitochondrial function. Identifying these mechanisms requires a flexible animal model that is well suited for "discovery experiments." The most promising model available today is the mitochondrial mutator mouse (Kujoth et al., 2005; Trifunovic et al., 2004). This mouse model carries an error-prone copy of DNA polymerase γ (*PolgA*^{D257A}), the enzyme that replicates the mitochondrial genome. Because of error-prone DNA replication, the *PolgA*^{D257} mice exhibit a >100-fold increase in mtDNA

This is an open access article under the CC BY-NC-ND license (http://creativecommons.org/licenses/by-nc-nd/4.0/).

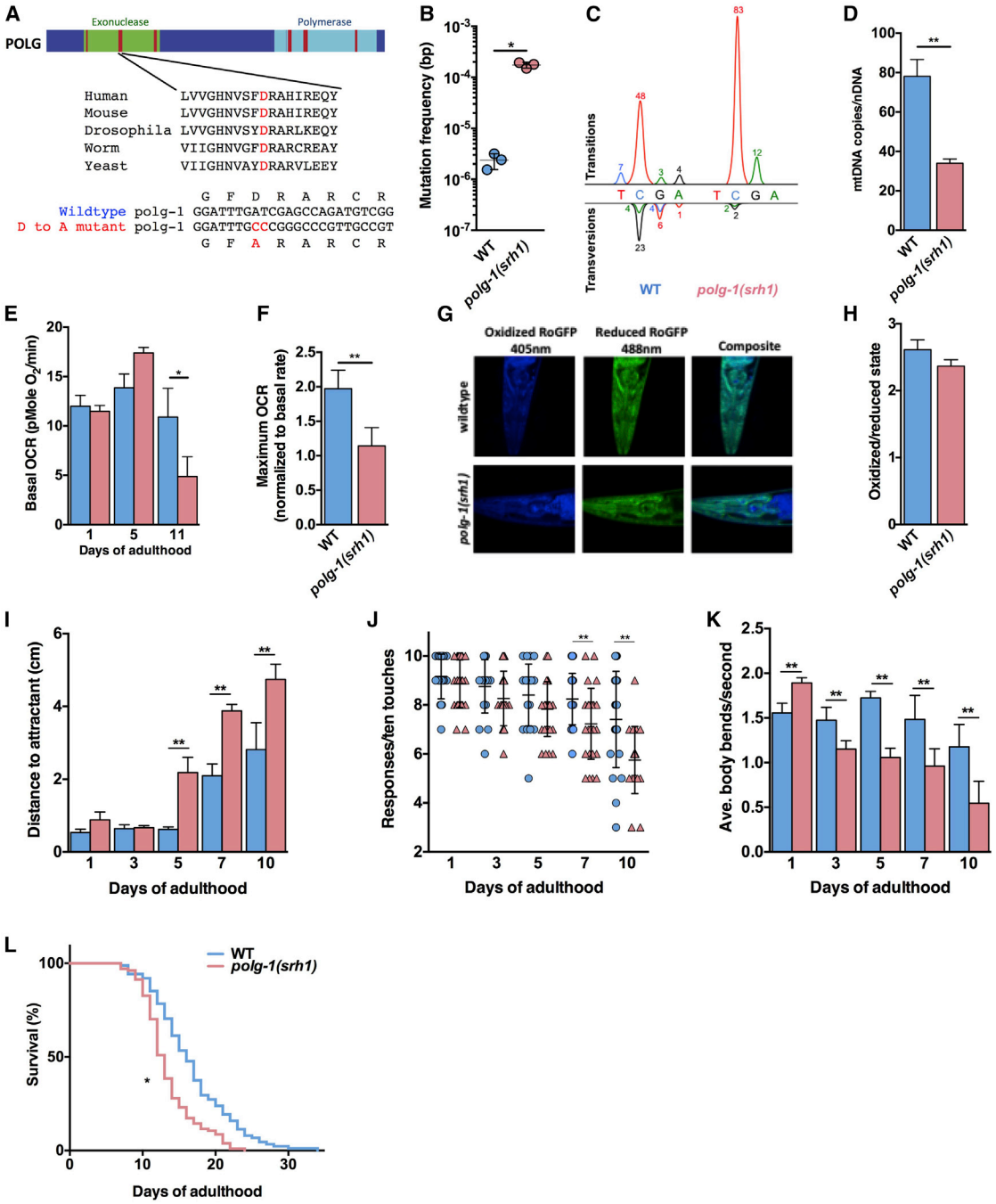

Figure 1. Characterization of the *polg-1(srh1)* Worms

(A) The exonuclease (green) domain of DNA polymerase γ contains three highly conserved regions (red) that control the fidelity of DNA synthesis, including an aspartic acid in exonuclease domain II that is essential for the proofreading activity of polymerase γ across the tree of life. We used CRISPR/Cas9 technology to mutate this residue to alanine in the error-prone allele *polg-1(srh1)*.

(B) The mtDNA mutation frequency of the *polg-1(srh1)* worms is >70-fold higher compared to WT worms.

(C) The mutation spectrum of WT and *polg-1(srh1)* depicted as peaks above and below the WT nucleotide according to standard electrophoretogram color coding (red, T; blue, C; black, G; green, A). The percentage of each type of mutation is listed by the peaks.

(D) The mtDNA copy number is reduced by 56% in the *polg-1(srh1)* worms.

(E) The basal respiration of *polg-1(srh1)* worms worsens with age compared to WT worms.

(F) The mitochondria of *polg-1(srh1)* worms display reduced reserve capacity upon FCCP treatment at 5 days of age.

(G and H) Confocal images of day 10 *polg-1(srh1)* and WT worms (G) do not reveal a significant difference in oxidation stress (H).

(legend continued on next page)

mutations, which results in extensive mtDNA disease (Kujoth et al., 2005; Trifunovic et al., 2004; Vermulst et al., 2007, 2008). However, logistical considerations prohibit these mice from being screened *en masse* to identify genes or molecular pathways that modulate their pathology. Therefore, we recreated the $PolgA^{D257A}$ mutation in *C. elegans*, a genetically tractable model organism that is amenable to high-throughput screens. Using CRISPR/Cas9 technology, we directly edited the *polg-1* gene (the *C. elegans* homolog of *PolgA*) and introduced the analogous D207A mutation (*polg-1(srh1)*) (Figure 1A). Similar to the mutator mice, we found that the *polg-1(srh1)* worms display a large increase in mtDNA mutations (Vermulst et al., 2007, 2008) (Figure 1B), which was primarily driven by C:G > T:A transitions (Figure 1C). These transitions were not equally distributed over the TaqI restriction site, despite the fact that it is a palindrome, suggesting that *polg-1*-mediated mutagenesis has a substantial strand bias (Figure 1C). Moreover, homozygous carriers of the *polg-1(srh1)* allele displayed a ~50% loss in mtDNA copy number (Figure 1D), mirroring the mtDNA depletion of homozygous mutator mice. Thus, even though mtDNA is replicated differently in worms compared to mice (Lewis et al., 2015), the *polg-1(srh1)* worms closely mimic the genetic instability of the mutator mice and display an increased rate of mtDNA mutation and depletion, two forms of mtDNA instability that cause mtDNA disease in humans (Copeland, 2008; El-Hattab and Scaglia, 2013).

Mutator Worms Replicate Major Hallmarks of mtDNA Disease in Humans

In human patients, mtDNA instability invariably results in mitochondrial dysfunction. To determine whether the mutator worms display mitochondrial dysfunction as well, we analyzed intact worms by respirometry. We found that at day 1 of adulthood, the mutator worms respire at the same rate as wild-type (WT) worms; however, at 11 days of age, they display a ~50% decrease in oxygen consumption (Figure 1E), indicating that they suffer from a progressive decline in mitochondrial function. Closer examination showed that this decline starts at 5 days of age, when basal respiration is optimal, but the reserve capacity of mitochondria has been reduced to 50% of WT levels (Figures 1F, S1A, and S1B). However, similar to the mutator mice, reduced respiration did not result in overt production of reactive oxidative species (Figures 1G, 1H, and S1C–S1F) (Kujoth et al., 2005; Trifunovic et al., 2005). The most prevalent symptom of inherited, as well as age-related mtDNA disease is neuromuscular dysfunction (Wallace, 2010). To determine whether the *polg-1(srh1)* worms display neuromuscular dysfunction as well, we tested their locomotion toward a chemo-attractant. This assay tests the ability of the worms to sense the chemo-attractant (Wes and Bargmann, 2001) (neuronal function), as well as their ability to crawl toward it (muscle function) (Kashyap et al., 2012). At day 1 of adulthood, the *polg-1(srh1)* worms were able to reach the chemo-attractant with the same efficiency as WT worms; however, as the *polg-1(srh1)* worms grew older, they became increasingly incapable of accomplishing this task (Figure 1I). On average, this phenotype emerged at 5 days of adulthood, coinciding with the onset of mitochondrial dysfunction, and worsened as the worms grew older (Figure 1I). To better understand the physiological underpinnings of this neuromuscular dysfunction, we used a "gentle touch" and "thrashing" assay. The gentle touch assay documents the ability of worms to detect a gentle tap on their head and their tail, which primarily tests the function of highly specialized mechanosensory neurons (Hobert et al., 1999). This assay revealed that the mutator worms are increasingly unresponsive to gentle touches, which became significantly different from WT worms at day 7 of adulthood and lasted until measurements concluded at day 10 (Figure 1J). The thrashing assay documents the number of times worms bend their bodies over in rapid succession in liquid media (Bansal et al., 2015; Han and Beckerle, 2009). Similar to the gentle touch assay, we found that the *polg-1(srh1)* worms display an age-related decrease in thrashing (Figure 1K; Movies S1 and S2). However, in contrast to the gentle touch assay, this phenotype was more severe and emerged concurrently with the chemotaxis defect at day 5 of adulthood. This observation suggests that the dysfunction of the *polg-1(srh1)* worms highlighted by the chemotaxis assay is most likely due to an inability to move, and not an inability to sense the chemoattractant. Further experimentation will be required to determine whether their inability to move is caused by dysfunction of the muscle cells themselves, or the motor neurons that innervate them. The neuromuscular dysfunction associated with mtDNA disease in humans is typically incompatible with normal lifespan (Wallace, 2005, 2010). To determine whether the *polg-1(srh1)* worms display a shortened lifespan as well, we compared the lifespan of WT worms to *polg-1(srh1)* worms and found that the *polg-1(srh1)* worms are indeed shorter lived than WT animals (Figure 1I), further confirming the extent of their disease, and their similarity to the short lived mutator mice (Trifunovic et al., 2004). Taken together, these experiments indicate that the *polg-1(srh1)* worms recapitulate several hallmarks of mtDNA disease in humans including increased mtDNA instability, loss of mitochondrial respiration, extensive neuromuscular dysfunction, and a shortened lifespan.

Mutation Load and Tissue Dysfunction of *polg-1(srh1)* Worms Worsen over Generations

The number of mutated mtDNA molecules that are transmitted from mother to child controls the severity and the type of pathology that emerges in children (Wallace, 2010). The higher this number is, the more complex the disease tends to be; however,

(I–K) Neuromuscular function assessed by chemotaxis (I), thrashing (J), and a gentle touch assay (K) reveals increased dysfunction in *polg-1(srh1)* worms compared to WT animals.

(L) The *polg-1(srh1)* worms have a median lifespan of 13 days compared to 16 days for WT worms (log-rank test $p < 0.01$).

Data for WT and *polg-1(srh1)* worms are in blue and pink, respectively (in B, D–F, and H–L).

Bar graphs represent the mean ± SEM of at least three biological replicates, and the lifespan assay was performed using at least 100 worms per genotype. Unpaired t tests were performed to determine significance (*$p < 0.05$, **$p < 0.01$; ns, no significant difference).

Also see Figure S1 and Movies S1 and S2.

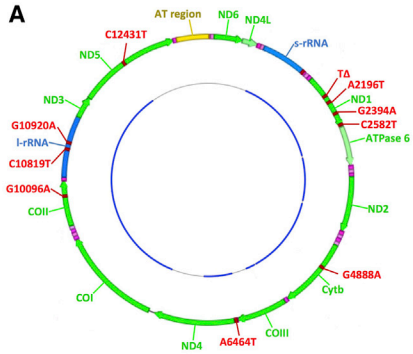

B

Generation	Mutation	Heteroplasmy	Gene	Change
5	-	-	-	-
15	G10096A	30%	COII	D to N
	G10920A	19%	1-rRNA	
25	C2582T	50%	ND1	L to F
	A6464T	40%	Thr tRNA	
	G10920A	38%	1-rRNA	
35	T2085	100%	ND1	early stop
	A2196T	9%	ND1	E to V
	G2394A	12%	ND1	R to K
	C2582T	91%	ND1	L to F
	G4888A	14%	Cytb	V to I
	A6464T	100%	Thr tRNA	
	C10819T	36%	l-rRNA	
	G10920A	25%	l-rRNA	
	C12431T	100%	ND5	S to L

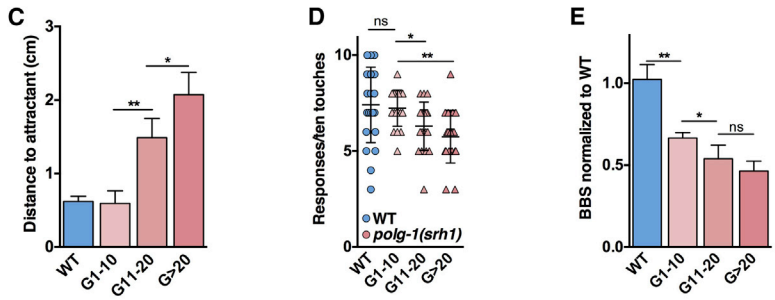

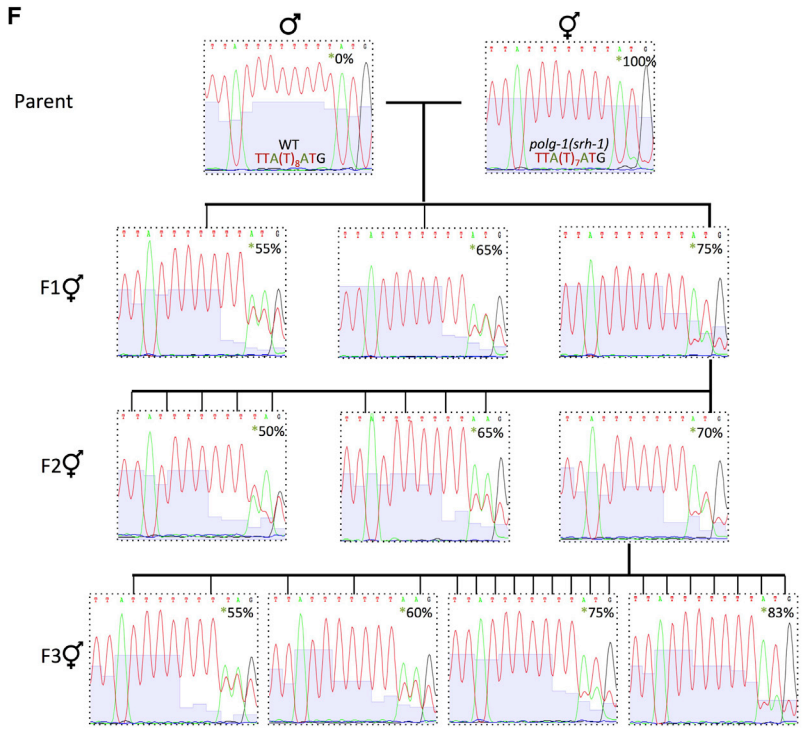

Figure 2. The Phenotype of the *polg-1(srh1)* Worms Worsens from Generation to Generation

(A) The outer circle represents the worm mitochondrial genome highlighting the protein-coding genes (green), rDNA (blue), AT-rich region (yellow), and all the mutations (red) that arose over 35 generations of maintaining the *polg-1(srh1)* mutator allele. The inner circle represents the regions that were sequenced (blue).

(B) mtDNA mutations were tracked over 35 generations in WT and *polg-1(srh1)* worms. At generations 5, 15, 25, and 35, ~11 kb of mtDNA of 3 progenies of a single WT and *polg-1(srh1)* worm were sequenced. The mutations depicted here were present in all 3 progenies, indicating that they were successfully transmitted through the germline. Three mutations, here denoted in purple, brown, and orange *polg-1(srh1)* were present across multiple generations and showed substantial genetic drift. No new mutations arose in the WT strain.

(C–E) Neuromuscular dysfunction was assessed by chemotaxis (C), thrashing (D), and gentle touch (E) revealed progressive dysfunction with increasing generation in the *polg-1(srh1)* worms.

(F) Representative electrophoretograms tracking the T2085 deletion that results in an early stop codon in the *ND1* gene in both the parent with *polg-1(srh1)* allele and its resultant progeny where the mutator allele has been mated out. Three individuals without the *polg-1(srh1)* allele in the F1 generation, 10 individuals in the F2 generations, and 21 individuals in the F3 generation were isolated and tested for the transmission of T2085 heteroplasmy in a background WT for *polg-1*.

Bar graphs represent the mean ± SEM of at least three biological replicates. Unpaired t tests were performed to determine significance (*$p < 0.05$, **$p < 0.01$; ns, no significant difference).

Also see Figure S2.

it has proven difficult to study germline transmission of mtDNA mutations in detail, because it is not possible to transform the mitochondrial genome at will. As a result, researchers are forced to rely on natural mtDNA variants to decipher the parameters that regulate mutation inheritance. We reasoned that the increased mutation rate of the *polg-1(srh1)* allele could greatly accelerate the process of isolating organisms with specific mtDNA mutations of interest, so that novel models of inherited mtDNA mutations can rapidly be generated. To test this hypothesis, we tracked the offspring of individual WT and *polg-1(srh1)* worms over 35 generations and sequenced the mtDNA of 3 siblings at generations 5, 15, 25, and 35. Over these generations, the mutator worms accrued an increasing number of detectable heteroplasmic mutations (Figures 2A, 2B, and S2), while the mtDNA of the WT worms remained pristine. Consistent with the idea that these mutations contribute to the dysfunction of the *polg-1(srh1)* worms, we found that the performance of the *polg-1(srh1)* worms in the chemotaxis (Figure 2C), gentle touch (Figure 2D) and thrashing (Figure 2E) assay decreased with increasing generation number. To prevent these generational effects from confounding our results, all studies were performed on generation-matched worms (generations 27–33).

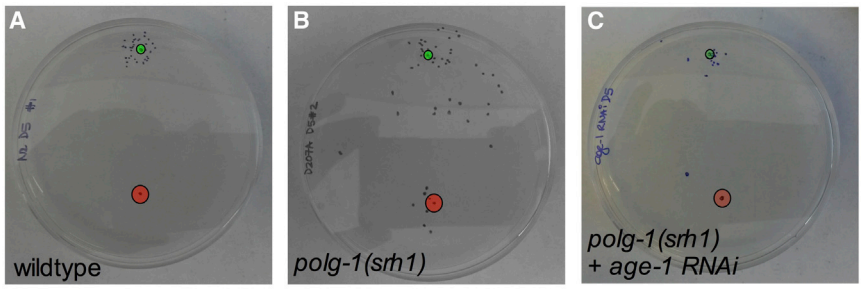

D

Gene	% Rescue	Protein Product	Pathway	
akt-1	56	serine/threonine kinase orthologous to human AKT1	IGF/Insulin Signaling	Lifespan determination and stress response
par-5	46	14-3-3 protein	IGF/Insulin Signaling	
age-1	35	phosphoinositide 3-kinase (PI3K)	IGF/Insulin Signaling	
rict-1	57	orthologous to mammalian RICTOR	TORC2	
lst-8	53	WD40 repeat-containing protein orthologous to yeast Lst8p	TOR	
egl-3	88	proprotein convertase orthologous to mammalian PCSK2	Peptide secretion	
ctl-1	45	cytosolic catalase	Stress Response	
bec-1	40	orthologous to mammalian BECN1	Autophagy	
lgg-1	30	orthologous to mammalian MAP-LC3	Autophagy	
unc-51	30	serine/threonine protein kinase orthologous to yeast Atg1p	Autophagy	
atp-3	77	subunit of the complex V	Electron Transport Chain	Mitochondrial function and homeostasis
D2030.4	66	subunit of the complex I	Electron Transport Chain	
T02H6.11	35	ubiquinol-cytochrome c reductase protein	Electron Transport Chain	
nuo-2	33	subunit of the mitochondrial complex I	Electron Transport Chain	
C33F10.12	53	solute carrier orthologous to human SLC25A3	Mitochondrial Solute Carriers	
K01C8.7	48	solute carrier orthologous to human SLC25A32	Mitochondrial Solute Carriers	
eat-3	32	mitochondrial dynamin orthologous to human OPA1	Mitochondrial Fusion	
mecr-1	70	mitochondrial trans-2-enoyl-CoA reductase	Fatty Acid Synthesis	
aco-2	31	aconitase orthologous to human ACO2	TCA Cycle	
spg-7	30	metalloprotease orthologous to human paraplegin, AFG3L2	Mitochondrial Proteostasis	
pdr-1	32	orthologous to human PARK2	Mitophagy	
dct-1	37	similar to mammalian BNIP3 proteins	Mitophagy & Apoptosis	
ced-3	39	caspase	Apoptosis	Misc.
cep-1	34	orthologous to human tumor suppressor TP53	Apoptosis	
nhr-32	41	orthologous to human PPARD, PPARG, and NR1D2	Hormone Receptor	

Figure 3. An RNAi Screen Identified Multiple Genes That Control mtDNA Disease in the *polg-1(srh1)* Worms

(A and B) 20–35 WT (A) and *polg-1(srh1)* (B) worms were aged for 5 days and spotted inside the red circle. A chemo-attractant was spotted 5 cm away from the worms (green circle), and the worms were allowed to crawl toward the chemo-attractant for 1 hr. Over this time span, most WT worms reached the chemo-attractant, while the *polg-1(srh1)* worms performed significantly worse.

(C) Twenty 5-day-old *polg-1(srh1)* adults on RNAi against *age-1* perform similar to WT worms.

(D) A list of genes that rescued the *polg-1(srh1)* neuromuscular defect by >30% when suppressed by RNAi.

See also Figure S3 and Table S1.

However, in some cases, the rationale of our experiments required a change in generation number. If so, this change has been clearly denoted. We further found that these germline mutations both increased and decreased over successive generations, indicating substantial genetic drift. To formally demonstrate that these mutations can be isolated to study their inheritance, we decided to remove the error-prone *polg-1(srh)* allele from the nuclear genome. We reasoned that this strategy would prevent additional mutations from accumulating in the mitochondrial genome, and allow desirable mtDNA mutations to be fixed in a WT nuclear background. To this end we crossed the mutagenic *polg-1(srh)* allele out of a worm that carried a single base-pair deletion in the ND1 gene (Figures 2A, 2B, and S2E). After the removal of the *polg-1(srh)* allele, we selectively picked individual progeny from parents with ~70% heteroplasmy over several generations (Figure 2F), and were able to successfully retain this mtDNA mutation. Interestingly, we found that, three generations after breeding out the mutator allele, 33% of the worms laid inviable embryos, 33% of the worms laid progeny that became larval phase 2 dauers, and 33% of the worms laid normal embryos that developed fully. This experiment demonstrates that it is possible to exploit the *polg-1(srh)* worms to generate novel animal models that display gross phenotypic abnormalities, and carry highly desirable mtDNA mutations in their germline, which could fill an important void in the mitochondrial research community.

Multiple Pathways Modulate mtDNA Disease in Worms

The chemotaxis assay described above is highly quantitative and reproducible, and tests the most important clinical aspects of mtDNA disease. Therefore, we used this assay as a screening tool to identify genes that can ameliorate the pathology associated with mtDNA disease (Figure 3). To this end, we performed a candidate RNAi screen using >130 RNAi constructs that control either *C. elegans* lifespan, overall health, or various aspects of mitochondrial function, parameters that are likely to intersect with mtDNA disease. We considered a gene a positive hit if RNAi against that gene improved the performance of the mutator worms by >30%. This cutoff is based on the observation that the inherent variation between randomly selected *polg-1(srh1)* worms rarely exceeded this threshold (0 out of 10 trials), indicating a <10% chance of discovering a false positive (Figure S3A). Second, RNAi against *age-1*, which we found to be a potent modulator of mtDNA disease (35% on average) (Figures 3A–3C), improved the performance of the mutator worms by >30% in 6 out of 9 trials (Figure S3B), indicating a > 60% chance of detecting a gene that increases the performance of the *polg-1(srh1)* worms by 35% or more. Excitingly, RNAi against numerous genes decreased the pathology associated with mtDNA disease in worms. For example, manipulation of the insulin growth factor (IGF)-1/insulin signaling (IIS) pathway, mitophagy, autophagy, apoptosis, and the mitochondrial unfolded protein response (UPR^{mt}) all ameliorated the neuromuscular defect of the *polg-1(srh1)* worms (Figure 3D). Interestingly, reduced autophagy was previously shown to ameliorate

mitochondrial dysfunction in a model of mitochondrial disease that is caused by a nuclear mutation (Peng et al., 2015), while suppression of apoptosis activates the highly beneficial stress response in worms (Judy et al., 2013). Similarly, mitophagy and UPR^{mt} are implicated in various diseases that contain a mitochondrial component (Haynes et al., 2013; Youle and Narendra, 2011). We frequently found that RNAi against multiple components of the same pathway rescued the mutator worms, strongly implicating that pathway in the progression of mtDNA disease (Figure 3D). Furthermore, we found that pathways that do not impact mitochondrial biology (such as the unfolded protein response of the ER) did not alter the performance of the mutator worms (Table S1). To validate the results of our screen and investigate the molecular mechanisms that underlie our observations, we picked three pathways that emerged from our screen and used drugs and genetic mutations to knockout or activate the molecular pathways they control.

The IGF-1/Insulin signaling pathway emerged as the strongest modulator of mtDNA disease, as RNAi against *age-1*, *par-5*, and *akt-1* all rescued the mobility defect of the *polg-1(srh1)* worms. In contrast, RNAi against *daf-18*, which directly opposes AGE-1 (Murphy and Hu, 2013), exacerbated the phenotype of the *polg-1(srh1)* worms (Table S1). At a mechanistic level, *age-1*, *par-5*, and *akt-1* share a common goal as well: they all increase the phosphorylation of the transcription factor DAF-16, trapping it in the cytoplasm and suppressing its activity (Murphy and Hu, 2013). RNAi against *age-1*, *par-5*, and *akt-1* releases this suppression and allows DAF-16 to translocate to the nucleus where it initiates a transcriptional program that promotes organismal health (Kenyon, 2010). Consistent with this idea, we found that RNAi against *daf-16* greatly exacerbated the neuromuscular defect of the *polg-1(srh1)* worms (Table S1). To verify our findings further, we introduced a hypomorph of the IGF-1/insulin receptor (*daf-2(e1370)*) into the *polg-1(srh1)* worms. This allele displays reduced IIS activity (Kenyon et al., 1993) and consistent with our RNAi results, we found that it rescued the neuromuscular defect of the mutator worms (Figure 4A). Conversely, a partial deletion of *daf-16* (*daf-16(mu86)*) exacerbated their phenotype (Figure 4B). Thus, these genetic mutations recapitulated the results of our RNAi screen. We further found that the *daf-2(e1370)* allele also improved the basal respiration rate of the mutator worms (Figure 4C), indicating that reduced IIS activity improves the mobility of the worms by correcting their underlying mitochondrial dysfunction. Interestingly, the *daf-2(e1370)* allele also improved mtDNA copy number in the mutator worms (Figure 4D), suggesting that it can partially rescue the etiology of the disease itself, although the mutation rate of the *polg-1(srh1)* worms was unaffected (Figure 4E).

Our screen further indicated that knockdown of *dct-1* and *pdr-1* could rescue the mobility defect of the mutator worms. Because these genes play a pivotal role in mitophagy (Palikaras et al., 2015), these results suggest that reduced mitophagy may be beneficial for the *polg-1(srh1)* worms. To verify these observations with a genetic mutant, we introduced the *pdr-1(gk448)* allele into the mutator worms. *Pdr-1* encodes the *C. elegans* homolog of the parkin ubiquitin ligase PARK2, and the *pdr-1(gk448)* allele carries a partial deletion that greatly reduces mitophagy in worms (Springer et al., 2005). Consistent with our RNAi screen, we found that the *pdr-1(gk448)* allele rescued the neuromuscular defect of the *polg-1(srh1)* worms (Figure 4F). Conversely, exposure of the mutator worms to urolithin A, a drug that induces mitophagy (Ryu et al., 2016), worsened their phenotype (Figure 4G). Finally, we found that the *pdr-1(gk448)* allele rescued the basal respiration rate of the mutator worms (Figure 4H), similar to the *daf-2(e1370)* allele. In contrast to the *daf-2(e1370)* allele though, we found that the *pdr-1(gk448)* allele did not alter mtDNA copy number (Figure 4I) and paradoxically increased the mitochondrial mutation frequency by 5.5-fold (Figure 4J).

Finally, our screen indicated that RNAi against the mitochondrial protease *spg-7* and several components of the electron transport chain *(atp-3, nuo-2, D2030.4,* and *T02H6.11)* rescued the neuromuscular defect of the mutator worms. Knockdown of *spg-7* or certain components of the electron transport chain are known to induce the unfolded protein response in mitochondria (Jovaisaite et al., 2014), indicating a possible involvement of this adaptive stress response in the rescue mechanism. Indeed, suppression of UPR^{mt} by RNAi against *haf-1*, *atfs-1*, and *ubl-5*, exacerbated the phenotype of the mutator worms (Table S1). To further verify the protective role of UPR^{mt} in mtDNA disease progression, we introduced the deletion allele *atfs-1(tm4919)* (Pellegrino and Haynes, 2015) into the *polg-1(srh1)* background. *Atfs-1* encodes a transcription factor required for UPR^{mt} activation. Interestingly, we found that homozygous carriers of the *atfs-1(tm4919)* allele rendered heterozygous *polg-1(srh1)* worms infertile, indicating that loss of UPR^{mt} greatly exacerbates the phenotype of the *polg-1(srh1)* worms. Accordingly, we were unable to generate homozygous *polg-1(srh1); atfs-1(tm4919)* worms for experiments. To answer the question of whether activation of this adaptive response is able to rescue mtDNA disease, we used a constitutively active *atfs-1* allele (*atfs-1(et15))* and found that it indeed partially rescued the neuromuscular defect of the mutator worms (Figure 4K). In addition, this allele rescued the decreased reserve capacity of mitochondria (Figure 4L) and slightly increased mtDNA copy number (Figure 4M), although it did not alter the mtDNA mutation frequency (Figure 4N).

DISCUSSION

MtDNA instability is associated with a remarkable number of human diseases. Although it is now possible to manage, and even improve some of the symptoms of mtDNA disease, there is currently no cure for either inherited mtDNA diseases or the mtDNA component of age-related diseases. To address this problem, we generated a model of mtDNA disease in *C. elegans,* which displays two forms of mtDNA instability known to cause mtDNA disease in humans: mtDNA depletion and mtDNA mutation. Both of these phenotypes are driven by a mutant DNA polymerase γ, which is a major source of mtDNA instability in patients as well. As a result, the *polg-1(srh1)* worms do not model any specific mtDNA disease, but serve as a general model of mtDNA disease caused by mtDNA instability. The *polg-1(srh1)* worms are especially useful because they can rapidly be screened for large numbers of genes, drugs, and small molecules that modulate mtDNA disease, which allows them to serve as a motor for discovery. Moreover, any findings can

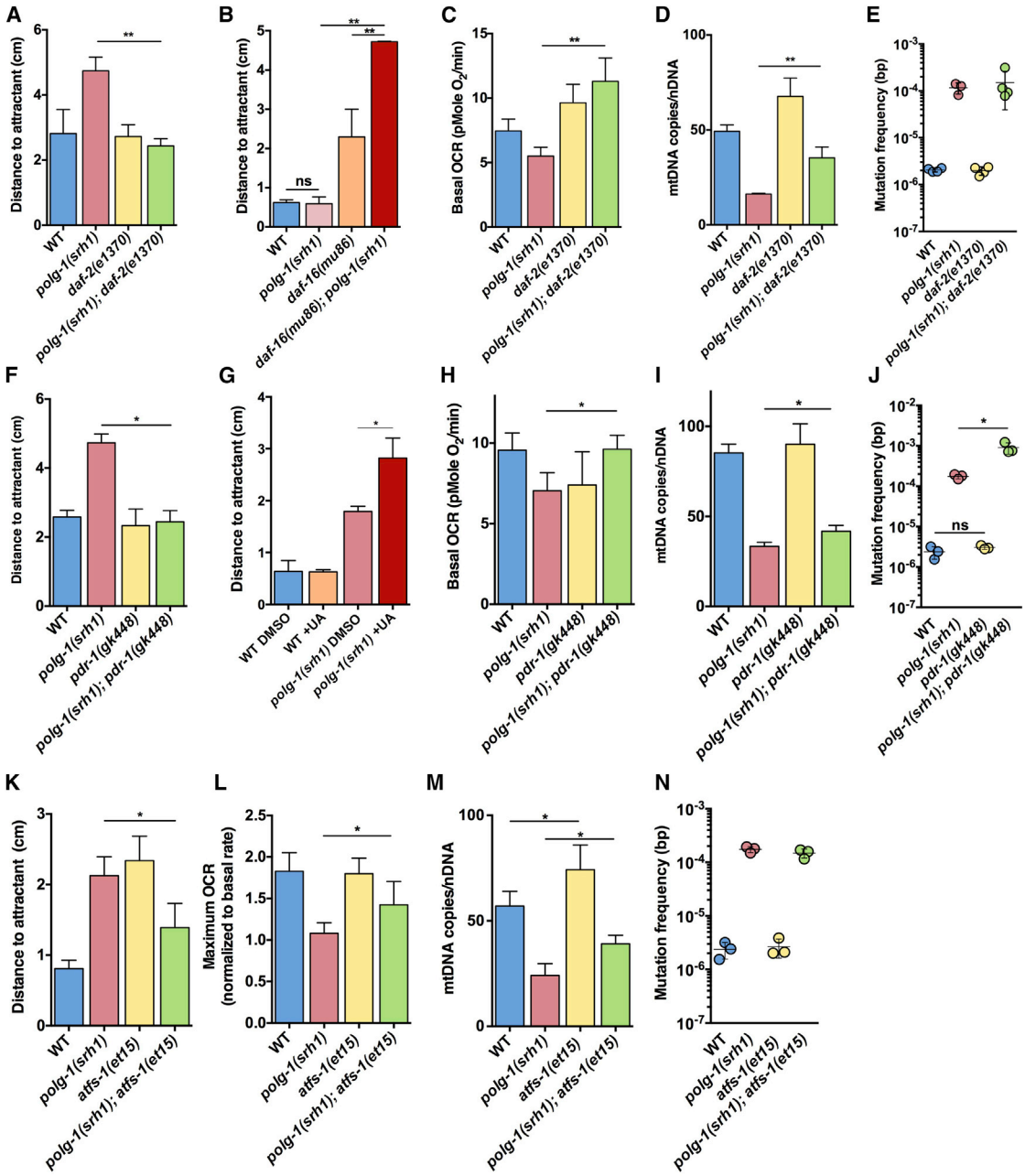

Figure 4. Verification of the RNAi Screen with Genetic Mutants and Small Molecules

(A) The *daf-2(e1370)* allele rescues the neuromuscular defect of 5-day-old *polg-1(srh1)* worms.

(B) The *daf-16(mu86)* allele worsens the neuromuscular defect of 5-day-old *polg-1(srh1)* worms. This set of experiments was performed at generation 7 instead of generation 30, when the phenotype of the mutator worms is not significantly different from the WT worms until 7 days of age. Accordingly, the detrimental effect of the *daf-16(mu86)* allele is better illustrated.

(C) The *daf-2(e1370)* allele rescues the basal respiration rate of 10-day-old *polg-1(srh1)* worms.

(D and E) The *daf-2(e1370)* allele (D) increases mtDNA copy number by 118%, but (E) has no effect on the mutation frequency of *polg-1(srh1)* worms.

(F) The *pdr-1(gk448)* allele rescues the chemotaxis defect of 5-day-old *polg-1(srh1)* worms.

(G) Induction of mitopagy with 50 μM urolithin A (UA) worsens the chemotaxis phenotype of the 5-day-old *polg-1(srh1)* worms.

(H) The *pdr-1(gk448)* allele rescues the basal respiration rate of 10-day-old *polg-1(srh1)* worms.

(I and J) The *pdr-1(gk448)* allele (I) increases mtDNA copy number by 25% and (J) results in a 5.5-fold increase in the mutation frequency of *polg-1(srh1)* worms.

(K and L) The *atfs-1(et15)* allele (K) rescues the chemotaxis defect of 5-day-old *polg-1(srh1)* worms and (L) the reserve capacity of 5-day-old *polg-1(srh1)* worms.

(M and N) The *atfs-1(et15)* allele (M) increases mtDNA copy number by 63%, but (N) has no effect on the mutation frequency of *polg-1(srh1)* worms.

Bar graphs represent the mean ± SEM of at least three biological replicates. Unpaired t tests were performed to determine significance (*$p < 0.05$, **$p < 0.01$; ns, no significant difference).

immediately be tested in the mitochondrial mutator mice to determine whether they are translatable to mammalian biology. Another useful feature of the mutator worms is that they rapidly accumulate mtDNA mutations in their germline, which allows for countless additional models of mtDNA disease to be generated. For example, after crossing the error-prone *polg-1(srh1)* allele out of the nuclear genome to prevent further mutation accumulation, worms with desirable germline mutations could be used to determine which parameters control the inheritance of mutated molecules. A similar approach was recently proposed for the mitochondrial mutator mice (Kauppila et al., 2016). Because mitochondrial research is greatly handicapped by a lack of inherited mutant mtDNA models, these worms would complement the mtDNA models that can be generated by restriction site targeting (Xu et al., 2008) to fill an important void in the research community.

A second problem that prevents the research community from developing a treatment for mtDNA disease is the lack of promising molecules to target. Here, we used the *polg-1(srh1)* worms to show that numerous molecular pathways control the severity of mtDNA disease. The most promising candidate we have identified thus far is the IGF-1/insulin signaling pathway. It has long been known that reduced IGF-1/insulin signaling has beneficial effects on the overall health of organisms (Kenyon, 2010); however, our results now suggest that for a discrete set of diseases, reduced IIS activity may also have a direct therapeutic application. Since reduced IIS activity increased mtDNA copy number, this approach may be especially useful for diseases caused by mtDNA depletion. Second, it is well known that reduced IGF-1 signaling is particularly beneficial to aging organisms (Kenyon, 2010). Since mtDNA mutations and mitochondrial dysfunction are associated with aging, these findings also provide insight into the molecular mechanisms by which reduced IGF-1 signaling prevents age-related dysfunction. We further found that reduced mitophagy could rescue the *polg-1(srh1)* worms from mtDNA disease, while increased mitophagy exacerbated their phenotype. This counter-intuitive observation suggests that while increased mitophagy is beneficial under normal circumstances, it can result in an adverse outcome in the context of disease. One potential explanation for this paradox could be that in the mutator worms recycled mitochondria are replaced with equally dysfunctional organelles, leading to futile cycles of mitophagy and mitochondrial biogenesis that results in further energy depletion. Interestingly, loss of PARK2 has both beneficial (reduced splenomegaly) and detrimental (*substantia nigra*) effects on the mutator mice (Pickrell and Youle, 2015), suggesting that the effect of reduced mitophagy on mammalian biology is highly cell-type and tissue specific. Another surprising observation was that reduced mitophagy increased the mutation burden of the mutator worms. These results suggest that mitophagy can potentially cull mutated mtDNA molecules from cells, which is consistent with the idea that mitophagy recycles dysfunctional organelles. Surprisingly though, knocking out PARK2 in the mitochondrial mutator mice did not seem to result in an increased mutation frequency. The reason for this discrepancy is currently unclear; however, an important difference between these organisms is that the mutator mice carry 10-fold more mutations than the mutator worms, which may limit the ability of mitophagy to significantly impact the mutation burden. Finally, we found that activation of UPR^{mt} could rescue the neuromuscular defect of the *polg-1(srh1)* worms. Interestingly, it was previously shown that a reduction in mtDNA copy number causes an imbalance in the number of proteins derived from the nuclear and mitochondrial genome. This imbalance causes proteotoxic stress inside mitochondria by preventing proteins from finding their natural binding partner, and UPR^{mt} ameliorates this stress. Since the *polg-1(srh1)* worms suffer from mtDNA depletion, we hypothesize that a reduction in proteotoxic stress partially underlies the improved performance of the *polg-1(srh1)*; *atfs-1(et15)* worms.

Taken together, these observations demonstrate that the *polg-1(srh1)* worms are a useful model to identify modulators of mtDNA disease. We further note that all of the modifiers we analyzed here seem to ameliorate mtDNA disease by improving mitochondrial function, suggesting that they could be beneficial for a broad range of mtDNA diseases. Moreover, since the genetic instability of the mutator worms is substantial, these modifiers are likely to be fairly powerful. It is further interesting to note that despite the fact that few targets are available today, a substantial number of genes can modulate the pathological consequences of mtDNA instability, suggesting that numerous targets may exist for therapeutic treatment of mtDNA disease. One potential conclusion from these observations is that precisely because energy is required for every biological process in our cells, multiple pathways may have evolved to manage or prevent mtDNA disease. Using the *polg-1(srh1)* worms, the mutator mice, and numerous other models that are still on the horizon, it now finally may be possible to identify these pathways in a reasonable period of time, which holds enormous promise for our ability to understand the molecular basis of mtDNA disease and to develop comprehensive treatment plans for patients.

EXPERIMENTAL PROCEDURES

Strains and Growth Conditions

The *polg-1(srh1)* worms were created using CRISPR/Cas9 technology in accordance with published protocols (Waaijers et al., 2013) and using the guide RNA sequence UGAUCGAGCCAGAUGUCGGG and the donor DNA sequence atcggagagattggaatggaaaaagtgattattggacataatgttggatttgCccgGg ccCgTtgCcgTgaggcttatcaatcgataaatgggtcaaagattcgatttatggatacaatgtct. Capitalized bases differ from the WT *polg-1* sequence. These changes were required for changing the aspartic acid at residue 207 to alanine, as well as inhibiting CRISPR/Cas9 cleavage after integration of the donor DNA. Additionally, these changes introduced a SmaI restriction site for genotyping purposes. Like in many other models of mitochondrial dysfunction, we found that the *polg-1(srh1)* worms displayed pronounced fertility problems when in a homozygous state. Therefore, we maintained the *polg-1(srh1)* allele as heterozygote animals with the balancer chromosome mnC1 that carries a pharyngeal fluorescent GFP reporter (CGC strain MT20110). Only the non-fluorescent homozygous worms were used for experiments. The *daf-2(e1370)*, *daf-16(mu86)*, *pdr-1(gk448)*, and *atfs-1(tm4919)* alleles were obtained from CGC, which is funded by NIH Office of Research Infrastructure Programs (P40 OD010440). The *atfs-1(et15)* strain was created by Dr. Marc Pilon (University of Gothenburg, Sweden) and was obtained from Dr. Cole Haynes. All strains were backcrossed into the laboratory N2 WT strain at least four times before comparative experiments were carried out. Strains were maintained without starvation at 20°C for at least two generations prior to experimental use. The L4 stage of worms was counted as day 0 of adulthood for all experiments.

mtDNA Copy Number

mtDNA copy number was determined by qPCR using at least three replicates per genotype by adapting a published protocol (Polyak et al., 2012). For each replicate, 10 L4 worms were collected in 10 μL of a buffer containing 10 mM Tris-HCl, 50 mM KCl, 1.5 mM $MgCl_2$, 0.001% gelatin, and 5 mg/mL Proteinase K. The worms were then incubated at 65°C for 75 min, followed by a 20-min incubation at 95°C, and diluted with 10 μL of H_2O. Subsequently, 5.5 μL of each sample was used to run a TaqMan assay with a Universal Master Mix (cat. no. 444040, Thermo Fisher Scientific), where ND4 (cat. no. 4440043, assay ID: AIFAT8G) and ACT-4 (assay ID: Ce02508047_s1, Thermo Fisher Scientific) assays quantified mtDNA and nDNA content, respectively. mtDNA copy numbers were then normalized to nDNA content.

Oxygen Consumption

To measure oxygen consumption, we adapted a published protocol (Dancy et al., 2016) and used approximately 300 L4 worms grown on plates to the appropriate age and collected them in M9 media (22 mM KH_2PO_4, 42 mM Na_2HPO_4, 86 mM NaCl, and 1 mM $MgSO_4$). The worms were washed 3 times and aliquoted over 3–5 wells of a 24-well plate from Seahorse Biosciences containing 500 μL of M9 media. Images were made of the wells to account for the exact number of worms deposited in each well, and the plates were analyzed with a Seahorse Biosciences XF24 Extracellular Flux Analyzer in accordance with the following program: 10 cycles of 2 min mixing, 2 min resting, and 2 min reading. This method demonstrates a linear increase in oxygen consumption rate (OCR) reading with increasing number of N2 and *polg-1(srh1)* worms (Figures S1A and S1B). To assess maximal respiration, we injected carbonyl cyanide-*4*-(trifluoromethoxy)phenylhydrazone (FCCP) to a final concentration 25 μM, and ten additional readings were made.

Oxidative State

For each data point, five age-matched worms with the *roGFP::orp1* construct were anesthetized on a 3% agarose pad with 10 mM levamisole-HCl, and their heads were imaged by excitation at 488 and 405 nm and emission at 500–600 nm. Confocal images were analyzed using ZEN Black software where the total fluorescence emitted by the excitation of each wavelength was calculated in arbitrary units (Figure S2C). Heads of WT and generation-matched *polg-1(srh1)* worms without the *roGFP::orp1* construct were imaged using the same experimental parameters to ascertain autofluorescence and correct the data (Figure S2D). The 405-nm fluorescence was divided by the fluorescence produced by 488 nm to ascertain the oxidative state of the animal. The average of the oxidative state of all animals in a group is reported. This method was adapted from a published protocol (De Henau et al., 2015). WT animals with the construct were treated with paraquat to ascertain the sensitivity of the construct (Figures S2E and S2F).

Chemotaxis

This protocol has been previously published (Kashyap et al., 2012; Wes and Bargmann, 2001). Briefly, 30 to 50 age-matched worms were collected and washed in M9 buffer. These worms were placed 5 cm away from a spot with 2 μL of 10% isoamyl alcohol in 100% ethanol and 1 μL 10% sodium azide. The worms were then allowed to crawl toward the chemo-attractant for 1 hr, after which the distance between the chemo-attractant and individual worms was noted and measured using ImageJ software. Studies involving urolithin A were performed by placing parents on plates containing 50 μM urolithin A. L4 progeny were collected on the third day and placed onto fresh plates with urolithin A every 2 days prior to chemotaxis on day 7.

Gentle Touch

Appropriately aged worms were gently touched with an eyelash attached to the end of a pick on their head and their tail. These touches were repeated 5 times for a total of ten touches, and any movement in the opposite direction was counted as a response. At least 20 worms were tracked longitudinally over a time span of 10 days, with measurements taken every 2 days (adapted from Hobert et al., 1999).

Thrashing

Thrashing assays were performed by placing 5–6 appropriately aged worms in a 25-μL drop of M9 buffer on a glass slide per movie. They were allowed to acclimate for 1 min, and then a 1 min long time-lapse movie was obtained at 16.7 frames per second. At least five movies using different sets of five individuals were made for each data point. Each movie was processed using the ImageJ plugin "wrmtrck" (Nussbaum-Krammer et al., 2015). The average body bends per second for each movie pertaining to a single genotype and age were averaged. Six to ten replicate movies were assayed per genotype and age.

Lifespan

For each strain, three replicates of at least 30 L4 worms were grown at 20°C and transferred onto fresh a plate every other day. Each day, the worms were observed to identify live and dead animals. Worms that were not visibly moving were gently prodded, observed for a response, and counted as dead if there was no response, after which they were removed from the plate. Worms that escaped or died due to bagging or bursting were omitted from the final analysis.

Mitochondrial Genome Sequencing

Single worms were boiled at 65°C for 75 min and 20 min at 95°C in 10 μL of buffer containing 10 mM Tris-HCl, 50 mM KCl, 1.5 mM $MgCl_2$, 0.001% gelatin, and 5 mg/mL Proteinase K. They were diluted with 10 μL of water, and four 100 μL PCR reactions were carried out per worms using Kapa HiFi polymerase (cat. no. KK2102, Kapa Biosystems) to amplify 11 kb of mitochondrial DNA (Figure S4A). Primer sequences and details for amplification cycling are denoted in Figure S4. The resultant electrophoretograms were scanned for double peaks to indicate heteroplasmic mutations arising in the mtDNA and aligned against WT mtDNA to identify homoplasmic mtDNA mutations.

Random Mutation Capture and Mutation Spectrum

The original protocol (Vermulst et al., 2007) was modified from using DNA isolated from mitochondrial preps to using whole-genome preps. Briefly, we sorted 2,000 homozygous *polg-1(srh1)* worms and performed whole-genome preps. 10–20 μg of total DNA was digested with Taq$^{\alpha}$I restriction enzyme (cat. no. R0149T, New England Biolabs) for 10 hr, with 1 μL of fresh enzyme added every hour. Digested DNA was amplified by qPCR or digital droplet PCR using two primer sets to measure total mtDNA copy number and mutant mtDNA copy number. PCR reactions across Taq$^{\alpha}$I sites that record mutant mtDNA molecules were digested with TaqαI post-PCR to determine that digestion was complete, and mtDNA mutation rates were calculated based on copy number measurements and qPCR efficiency.

Control Primers

Forward: gagcgtcatttattgggaaga
Reverse: aataaagcttgtgctaatcccat

TaqI Primers

Forward: acaccggtgaggtctttggttcat
Reverse: aacctaagccctaggcccaaagtaac

To separate the individual mutations, amplicons were diluted to a single-molecule level and PCR amplified separately and then sequenced.

RNAi

We used RNAi constructs from the Arhinger library and adapted the protocol from the Ahringer laboratory (Kamath and Ahringer, 2003). For RNAi treatments, WT or *polg-1(srh1)* heterozygote parents were placed on plates spotted with bacteria that had the L4440 (no RNAi) or RNAi construct of interest. On the third day, L4 progeny were placed on fresh L4440 or RNAi plates and transferred to fresh plates on days 2 and 4. If the RNAi caused any developmental defects, then L4 progeny from the L4440 plates were placed on the RNAi plates. On the fifth day of the adulthood, the chemotaxis assay was performed as described above.

SUPPLEMENTAL INFORMATION

Supplemental Information includes four figures, one table, and two movies and can be found with this article online at https://doi.org/10.1016/j.celrep.2018.02.099.

ACKNOWLEDGMENTS

We would like to thank Marni J. Falk, Douglas C. Wallace, and Robert B. Wilson for comments on the manuscript and the project design. This work was supported by grants from the NIH (R01-GM124532 to M.V.; CA204894 and ES026222 to J.H.B.), a grant from NIEHS (T32-ES019851 to C.F.), and a pilot award from UPenn (FP20457 to M.V.). The contents of this publication do not necessarily represent the official views of the NIH.

AUTHOR CONTRIBUTIONS

S.H. and M.V. conceived the project. S.H., N.G.E., and J.H.B. performed the mutation frequency analyses. S.H. and J.L.W. determined the mutation spectrum. A.L. performed the oxidative state studies. S.H., A.L., and C.F. carried out the mobility assays. S.H. generated the strains, performed the gentle touch, thrashing, and lifespan studies, and analyzed worm mtDNA over multiple generations. C.M.H., B.P.B., J.A.-F., and T.G. provided worm strains, technical expertise, and analysis tools. S.H. and M.V. wrote the manuscript. All authors contributed to and commented on this manuscript.

DECLARATION OF INTERESTS

The authors declare no competing interests.

Received: July 5, 2017
Revised: December 7, 2017
Accepted: February 25, 2018
Published: March 20, 2018

REFERENCES

Anderson, S., Bankier, A.T., Barrell, B.G., de Bruijn, M.H., Coulson, A.R., Drouin, J., Eperon, I.C., Nierlich, D.P., Roe, B.A., Sanger, F., et al. (1981). Sequence and organization of the human mitochondrial genome. Nature *290*, 457–465.

Bansal, A., Zhu, L.J., Yen, K., and Tissenbaum, H.A. (2015). Uncoupling lifespan and healthspan in Caenorhabditis elegans longevity mutants. Proc. Natl. Acad. Sci. USA *112*, E277–E286.

Copeland, W.C. (2008). Inherited mitochondrial diseases of DNA replication. Annu. Rev. Med. *59*, 131–146.

Dancy, B.M., Brockway, N., Ramadasan-Nair, R., Yang, Y., Sedensky, M.M., and Morgan, P.G. (2016). Glutathione S-transferase mediates an ageing response to mitochondrial dysfunction. Mech. Ageing Dev. *153*, 14–21.

De Henau, S., Tilleman, L., Vangheel, M., Luyckx, E., Trashin, S., Pauwels, M., Germani, F., Vlaeminck, C., Vanfleteren, J.R., Bert, W., et al. (2015). A redox signalling globin is essential for reproduction in Caenorhabditis elegans. Nat. Commun. *6*, 8782.

El-Hattab, A.W., and Scaglia, F. (2013). Mitochondrial DNA depletion syndromes: review and updates of genetic basis, manifestations, and therapeutic options. Neurotherapeutics *10*, 186–198.

Han, H.F., and Beckerle, M.C. (2009). The ALP-enigma protein ALP-1 functions in actin filament organization to promote muscle structural integrity in Caenorhabditis elegans. Mol. Biol. Cell *20*, 2361–2370.

Haynes, C.M., Fiorese, C.J., and Lin, Y.F. (2013). Evaluating and responding to mitochondrial dysfunction: the mitochondrial unfolded-protein response and beyond. Trends Cell Biol. *23*, 311–318.

Hobert, O., Moerman, D.G., Clark, K.A., Beckerle, M.C., and Ruvkun, G. (1999). A conserved LIM protein that affects muscular adherens junction integrity and mechanosensory function in Caenorhabditis elegans. J. Cell Biol. *144*, 45–57.

Jovaisaite, V., Mouchiroud, L., and Auwerx, J. (2014). The mitochondrial unfolded protein response, a conserved stress response pathway with implications in health and disease. J. Exp. Biol. *217*, 137–143.

Judy, M.E., Nakamura, A., Huang, A., Grant, H., McCurdy, H., Weiberth, K.F., Gao, F., Coppola, G., Kenyon, C., and Kao, A.W. (2013). A shift to organismal stress resistance in programmed cell death mutants. PLoS Genet. *9*, e1003714.

Kamath, R.S., and Ahringer, J. (2003). Genome-wide RNAi screening in Caenorhabditis elegans. Methods *30*, 313–321.

Kashyap, L., Perera, S., and Fisher, A.L. (2012). Identification of novel genes involved in sarcopenia through RNAi screening in Caenorhabditis elegans. J. Gerontol. A Biol. Sci. Med. Sci. *67*, 56–65.

Kauppila, J.H.K., Baines, H.L., Bratic, A., Simard, M.L., Freyer, C., Mourier, A., Stamp, C., Filograna, R., Larsson, N.G., Greaves, L.C., and Stewart, J.B. (2016). A Phenotype-driven approach to generate mouse models with pathogenic mtDNA mutations causing mitochondrial disease. Cell Rep. *16*, 2980–2990.

Kenyon, C.J. (2010). The genetics of ageing. Nature *464*, 504–512.

Kenyon, C., Chang, J., Gensch, E., Rudner, A., and Tabtiang, R. (1993). A C. elegans mutant that lives twice as long as wild type. Nature *366*, 461–464.

Kraytsberg, Y., Kudryavtseva, E., McKee, A.C., Geula, C., Kowall, N.W., and Khrapko, K. (2006). Mitochondrial DNA deletions are abundant and cause functional impairment in aged human substantia nigra neurons. Nat. Genet. *38*, 518–520.

Kujoth, G.C., Hiona, A., Pugh, T.D., Someya, S., Panzer, K., Wohlgemuth, S.E., Hofer, T., Seo, A.Y., Sullivan, R., Jobling, W.A., et al. (2005). Mitochondrial DNA mutations, oxidative stress, and apoptosis in mammalian aging. Science *309*, 481–484.

Lewis, S.C., Joers, P., Willcox, S., Griffith, J.D., Jacobs, H.T., and Hyman, B.C. (2015). A rolling circle replication mechanism produces multimeric lariats of mitochondrial DNA in Caenorhabditis elegans. PLoS Genet. *11*, e1004985.

Murphy, C.T., and Hu, P.J. (2013). Insulin/insulin-like growth factor signaling in C. elegans. In WormBook: The Online Review of C. elegans Biology, ed., D.M. Eisenmann, ed. (The C. elegans Research Community). https://doi.org/10.1895/wormbook.1.7.1. https://www.ncbi.nlm.nih.gov/books/NBK179230/.

Nussbaum-Krammer, C.I., Neto, M.F., Brielmann, R.M., Pedersen, J.S., and Morimoto, R.I. (2015). Investigating the spreading and toxicity of prion-like proteins using the metazoan model organism C. elegans. J. Vis. Exp. *95*, 52321.

Palikaras, K., Lionaki, E., and Tavernarakis, N. (2015). Balancing mitochondrial biogenesis and mitophagy to maintain energy metabolism homeostasis. Cell Death Differ. *22*, 1399–1401.

Pellegrino, M.W., and Haynes, C.M. (2015). Mitophagy and the mitochondrial unfolded protein response in neurodegeneration and bacterial infection. BMC Biol. *13*, 22.

Peng, M., Ostrovsky, J., Kwon, Y.J., Polyak, E., Licata, J., Tsukikawa, M., Marty, E., Thomas, J., Felix, C.A., Xiao, R., et al. (2015). Inhibiting cytosolic translation and autophagy improves health in mitochondrial disease. Hum. Mol. Genet. *24*, 4829–4847.

Pickrell, A.M., and Youle, R.J. (2015). The roles of PINK1, parkin, and mitochondrial fidelity in Parkinson's disease. Neuron *85*, 257–273.

Polyak, E., Zhang, Z., and Falk, M.J. (2012). Molecular profiling of mitochondrial dysfunction in Caenorhabditis elegans. Methods Mol. Biol. *837*, 241–255.

Ryu, D., Mouchiroud, L., Andreux, P.A., Katsyuba, E., Moullan, N., Nicolet-Dit-Félix, A.A., Williams, E.G., Jha, P., Lo Sasso, G., Huzard, D., et al. (2016). Urolithin A induces mitophagy and prolongs lifespan in C. elegans and increases muscle function in rodents. Nat. Med. *22*, 879–888.

Saneto, R.P., and Sedensky, M.M. (2013). Mitochondrial disease in childhood: mtDNA encoded. Neurotherapeutics *10*, 199–211.

Springer, W., Hoppe, T., Schmidt, E., and Baumeister, R. (2005). A Caenorhabditis elegans Parkin mutant with altered solubility couples alpha-synuclein aggregation to proteotoxic stress. Hum. Mol. Genet. *14*, 3407–3423.

Trifunovic, A., Wredenberg, A., Falkenberg, M., Spelbrink, J.N., Rovio, A.T., Bruder, C.E., Bohlooly-Y, M., Gidlöf, S., Oldfors, A., Wibom, R., et al. (2004). Premature ageing in mice expressing defective mitochondrial DNA polymerase. Nature *429*, 417–423.

Trifunovic, A., Hansson, A., Wredenberg, A., Rovio, A.T., Dufour, E., Khvorostov, I., Spelbrink, J.N., Wibom, R., Jacobs, H.T., and Larsson, N.G. (2005). Somatic mtDNA mutations cause aging phenotypes without affecting reactive oxygen species production. Proc. Natl. Acad. Sci. USA *102*, 17993–17998.

Vermulst, M., Bielas, J.H., Kujoth, G.C., Ladiges, W.C., Rabinovitch, P.S., Prolla, T.A., and Loeb, L.A. (2007). Mitochondrial point mutations do not limit the natural lifespan of mice. Nat. Genet. *39*, 540–543.

Vermulst, M., Wanagat, J., Kujoth, G.C., Bielas, J.H., Rabinovitch, P.S., Prolla, T.A., and Loeb, L.A. (2008). DNA deletions and clonal mutations drive premature aging in mitochondrial mutator mice. Nat. Genet. *40*, 392–394.

Waaijers, S., Portegijs, V., Kerver, J., Lemmens, B.B., Tijsterman, M., van den Heuvel, S., and Boxem, M. (2013). CRISPR/Cas9-targeted mutagenesis in Caenorhabditis elegans. Genetics *195*, 1187–1191.

Wallace, D.C. (2005). A mitochondrial paradigm of metabolic and degenerative diseases, aging, and cancer: a dawn for evolutionary medicine. Annu. Rev. Genet. *39*, 359–407.

Wallace, D.C. (2010). Mitochondrial DNA mutations in disease and aging. Environ. Mol. Mutagen. *51*, 440–450.

Wanagat, J., Cao, Z., Pathare, P., and Aiken, J.M. (2001). Mitochondrial DNA deletion mutations colocalize with segmental electron transport system abnormalities, muscle fiber atrophy, fiber splitting, and oxidative damage in sarcopenia. FASEB J. *15*, 322–332.

Wes, P.D., and Bargmann, C.I. (2001). C. elegans odour discrimination requires asymmetric diversity in olfactory neurons. Nature *410*, 698–701.

Xu, H., DeLuca, S.Z., and O'Farrell, P.H. (2008). Manipulating the metazoan mitochondrial genome with targeted restriction enzymes. Science *321*, 575–577.

Youle, R.J., and Narendra, D.P. (2011). Mechanisms of mitophagy. Nat. Rev. Mol. Cell Biol. *12*, 9–14.

Cell Reports, Volume *22*

Supplemental Information

Multiple Molecular Mechanisms Rescue mtDNA Disease in *C. elegans*

Suraiya Haroon, Annie Li, Jaye L. Weinert, Clark Fritsch, Nolan G. Ericson, Jasmine Alexander-Floyd, Bart P. Braeckman, Cole M. Haynes, Jason H. Bielas, Tali Gidalevitz, and Marc Vermulst

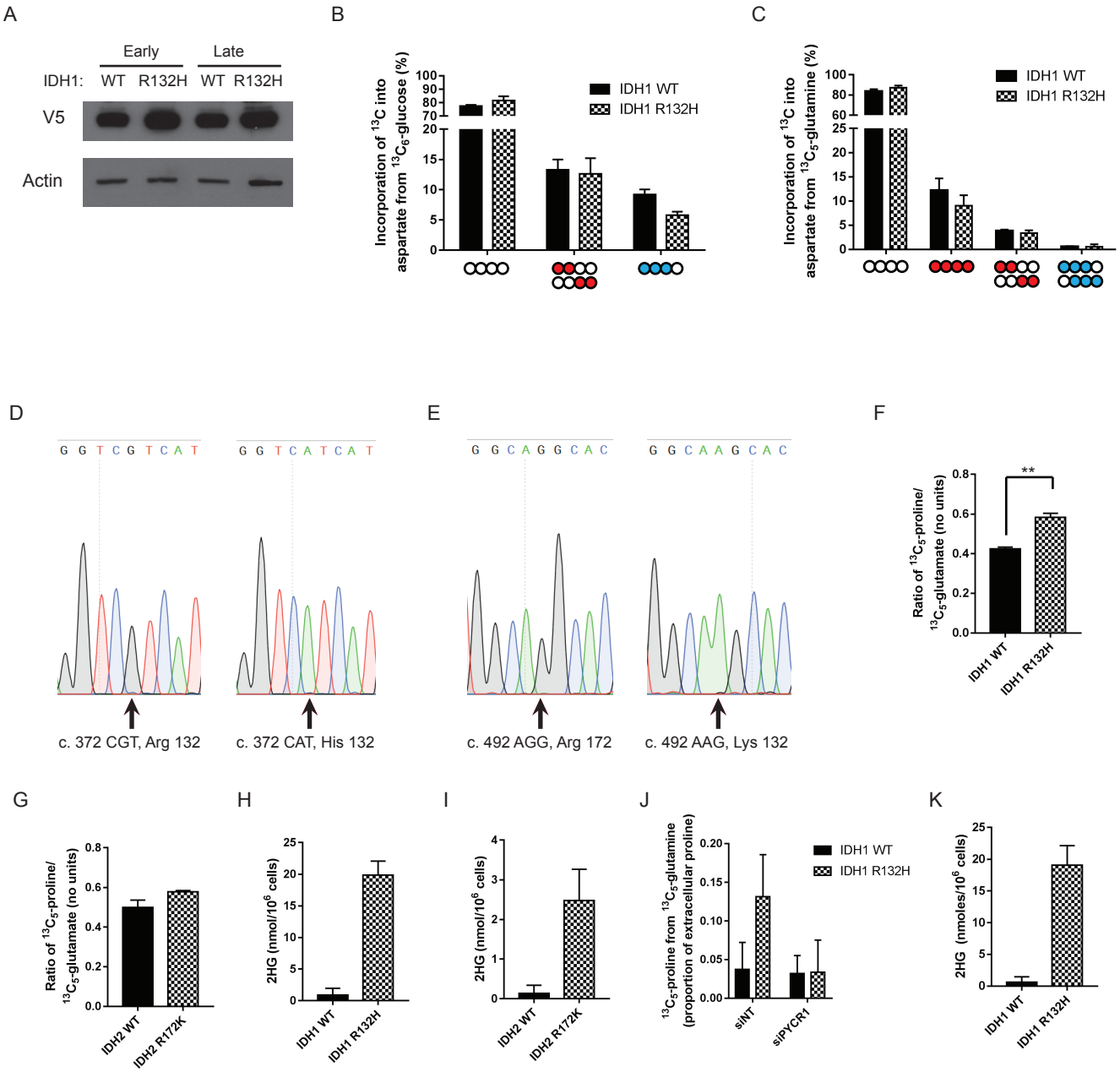

Figure S1A, Related to Figure 1. Expression of the V5-tagged IDH1 WT and R132H constructs is similar between the paired lines, and remains constant with continuous culture. **B:** Incorporation of ^{13}C from $^{13}C_6$-glucose into aspartate through oxidative pathways (red) is unchanged between IDH1 WT and IDH1 R132H-expressing cells. **C:** ^{13}C incorporation from $^{13}C_5$-glutamine into aspartate is unchanged between IDH1 WT and R132H-expressing cells. **D:** Sequencing results confirming successful transduction of R132H-mutated IDH1 (right) into LN18 parental cell lines (left). **E:** As for (**D**), but IDH2 R172K. Synthesis of proline from glutamate is increased in an IDH1 R132H-expressing (**F**), but not IDH2 R172K-expressing (**G**) LN18 cell line. Expression of IDH1 R132H (H) or R172K (**I**) in the LN18 parental cell line results in increased extracellular 2HG levels. **J:** IDH1 R132H-expressing HOG cells demonstrate increased PYCR1-mediated proline synthesis and excretion in the presence of exogenous 200 μM proline. Data presented show extracellular $^{13}C_5$-proline as a proportion of total extracellular proline. **K:** 2HG excreted into the medium in early passage IDH1 R132H-expressing HOG cell line is around 20-fold greater than in IDH1 WT-expressing controls.

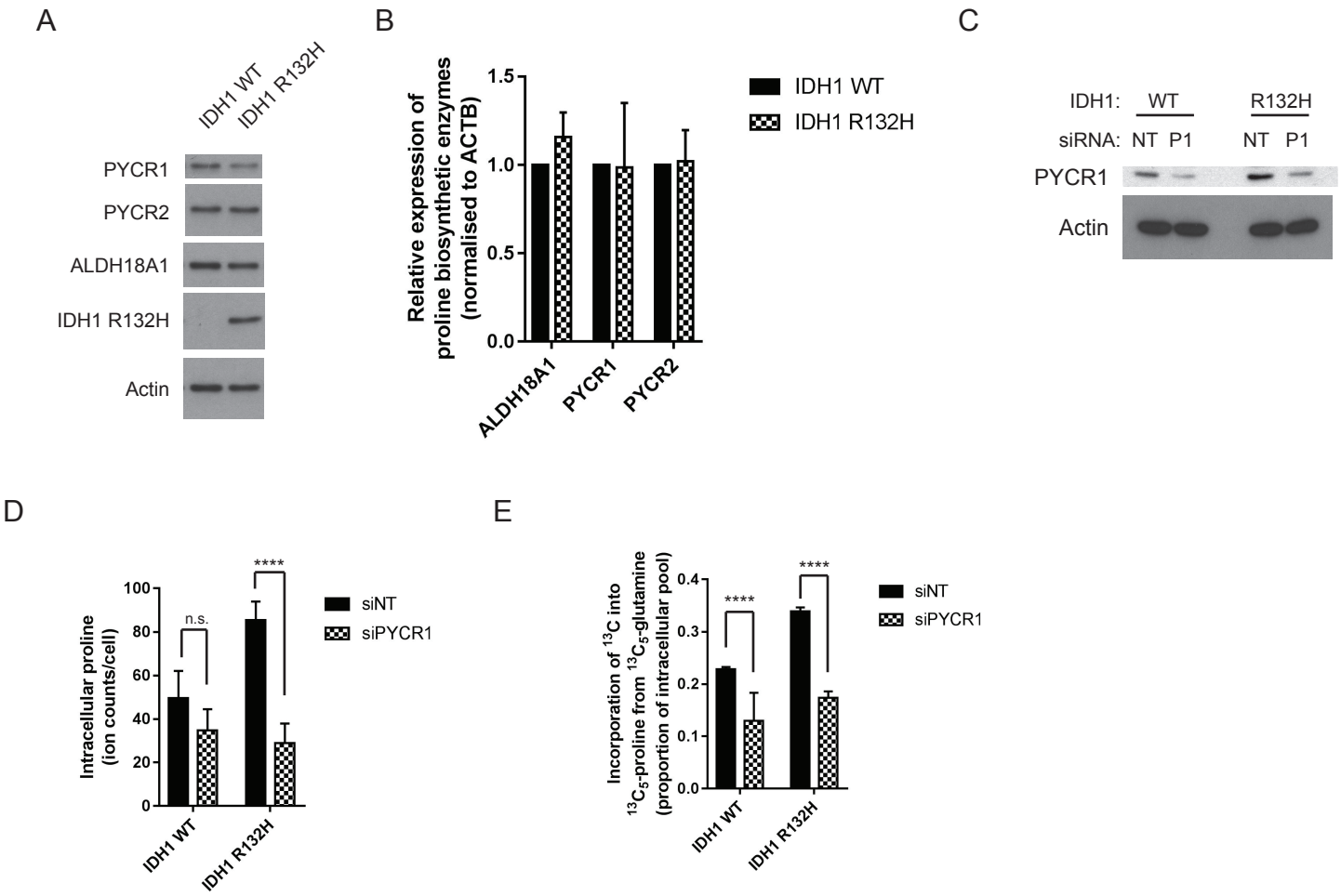

Figure S2A, Related to Figure 2: LN18 IDH1 R132H-expressing cells do not demonstrate increased expression in proline biosynthetic enzymes. **B:** Relative mRNA expression of the three mitochondrial proline biosynthetic enzymes, ALDH18A1 (pyrroline 5-carboxylate synthetase), PYCR1 and PYCR2 shows that there is no difference between the IDH1 WT and IDH1 R132H-expressing HOG cells. **C:** Immunoblot showing successful knockdown of PYCR1 in LN18 cells. **D:** LN18 cells expressing IDH1 R132H synthesize increased proline from glutamine (**E**) through PYCR1. '****' indicates $p<0.0001$, using a 2-way ANOVA with Sidak's multiple comparisons test.

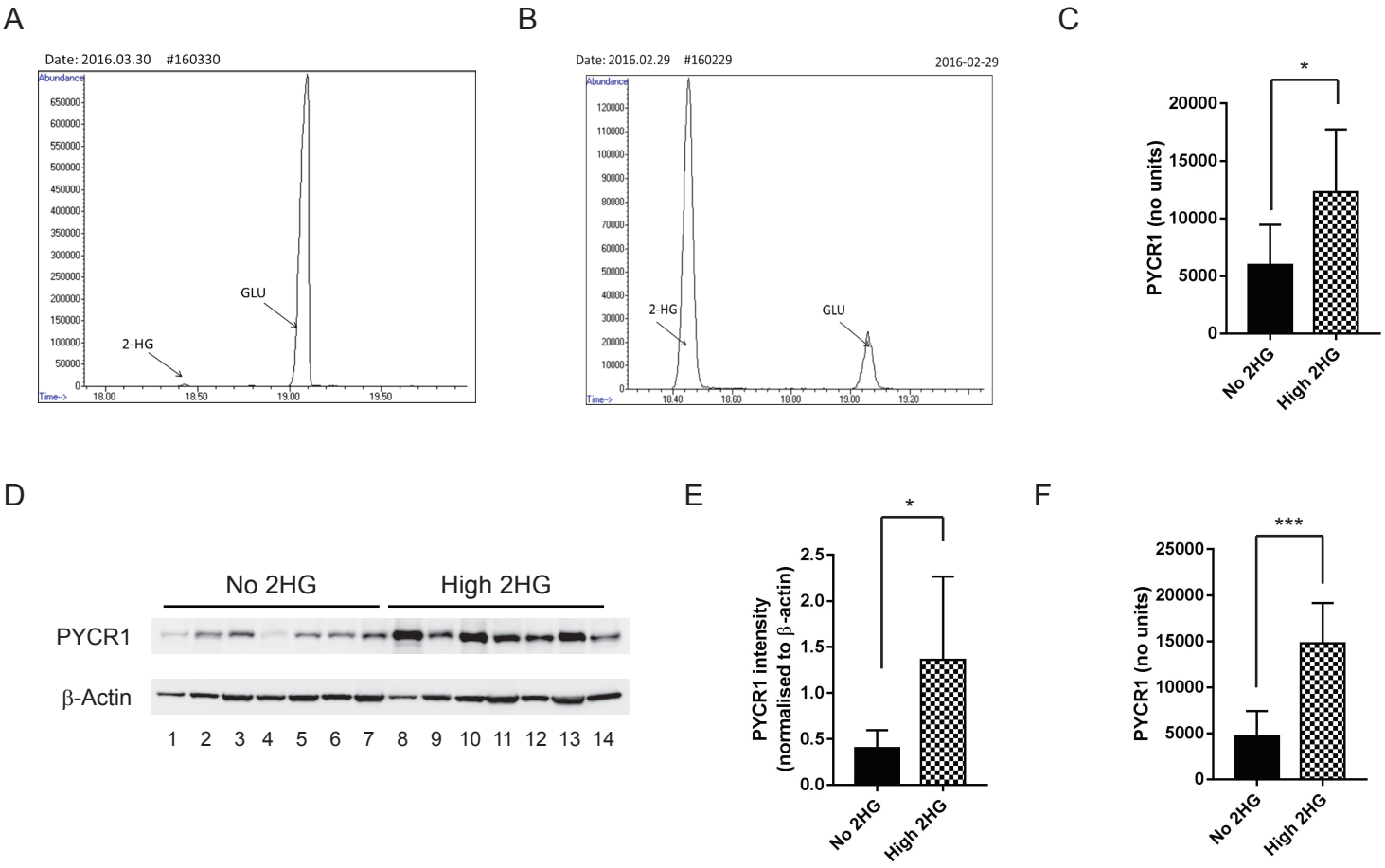

Figure S3A and B, Related to Figure 3: Representative spectra from GC-MS analysis of gliomas showing a 'no 2HG' (**A**) and high 2HG (**B**) sample. The ion at m/z 433 was used, with glutamate retention used as a control. **C:** PYCR1 densitometry normalised to protein loaded. **D:** Additional glioma samples blotted for PYCR1 (Figure 3C), separated by their tumoral 2HG levels, showing increased expression of PYCR1 both normalised to actin (**E**) and normalised to total protein loaded (**F**).

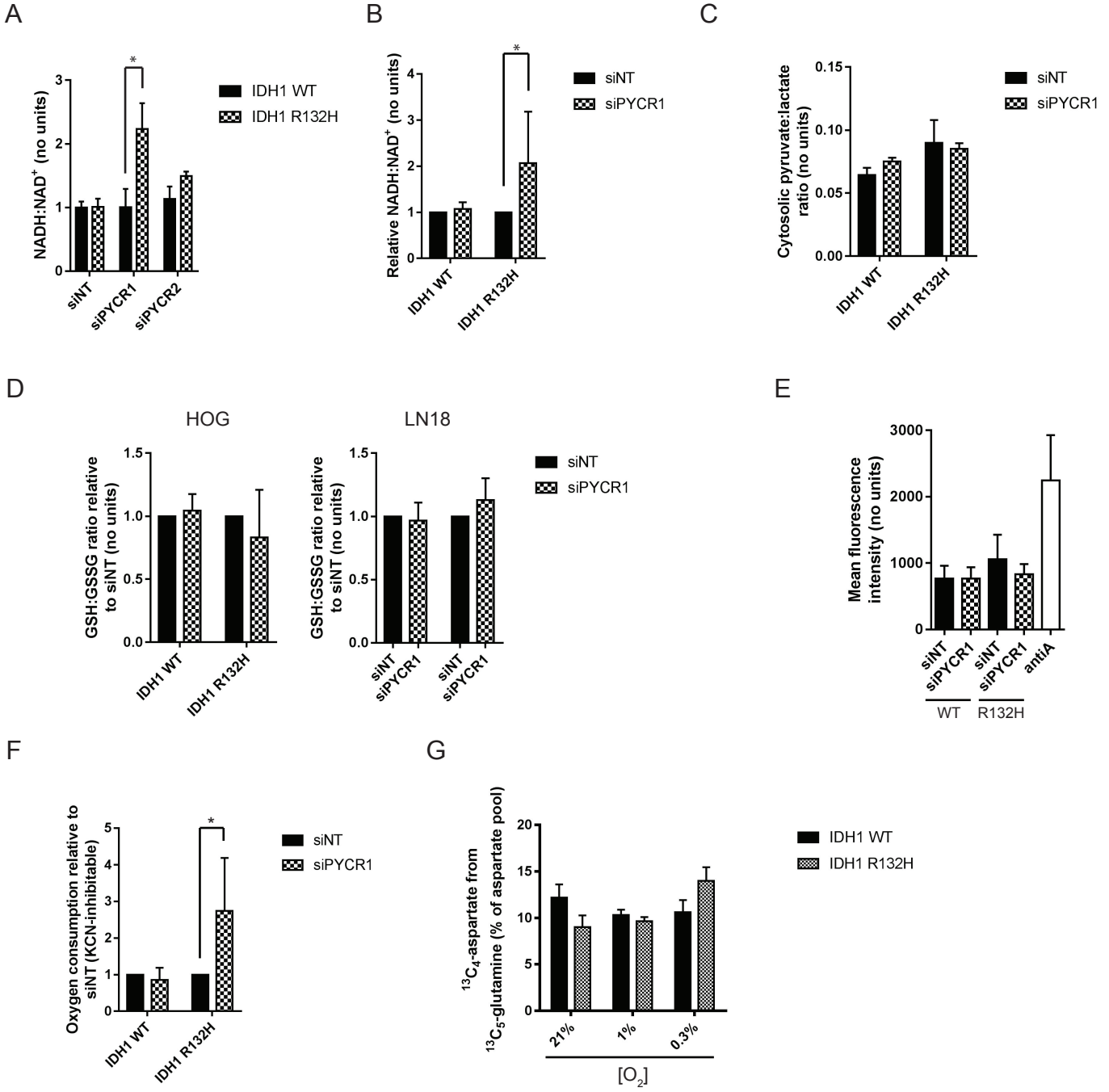

Figure S4A and B, Related to Figure 4: Knockdown of PYCR1 alters the NAD^+:NADH ratio in IDH1 R132H-expressing HOG (**A**) and LN18 (**B**) cells. No change is observed in IDH1 WT cells. '*' $p<0.05$, 2-way ANOVA with post-test. **C:** In common with the R132H-expressing HOG cells, cytosolic pyruvate:lactate ratio is unchanged after siPYCR1 in LN18 cell line. **D:** PYCR1 knockdown does not significantly alter the GSH:GSSG ratio in either wild-type or IDH1 R132H-expressing HOG (left) or LN18 (right) cells. **E:** siPYCR1 does not alter mitochondrial ROS production as measured using mitoSOX. AntiA, antimycin A positive control treatment of IDH1 WT cells. **F:** Knockdown of PYCR1 in R132H-expressing LN18 cells results in increased respiration. **G:** Oxidative aspartate synthesis is maintained in IDH1 R132H-expressing cells in limiting oxygen tensions compared with IDH1 WT cells.

Table S1

Lane # on Figure 3C	Age	Gender	Diagnosis	Sequencing	IHC for IDH1(H09)
1	62	M	GBM	Wild Type	(−)
2	64	M	GBM	Wild Type	(−)
3	46	M	AA	Wild Type	(−)
4	44	M	GBM	Wild Type	(−)
5	39	F	Oligodendroglioma	Wild Type	(−)
6	41	F	GBM	Wild Type	(−)
7	52	M	GBM	Wild Type	(−)
8	27	M	Astrocytoma	IDH1 R132H	(+)
9	50	M	Oligoastrocytoma	IDH1 R132H	(+)
10	32	F	Astrocytoma	IDH1 R132H	(+/−)
11	27	F	Astrocytoma	IDH1 R132H	(−)
12	39	F	Astrocytoma	IDH1 R132H	(+)
13	50	M	AA	IDH1 R132H	(+/−)
14	31	F	GBM	IDH1 R132H	(+)

Table S1, Related to Figure 3C: Patient characteristics for samples used in Figure 3C. Abbreviations: AA; Anaplastic astrocytoma, AO; Anaplastic oligodendroglioma, AOA; Anaplastic oligoastrocytoma, GBM; Glioblastoma.

Table S2

Diagnosis	Age	Gender	2-HG AUC	Proline AUC
AA	50	M	1220042	1337921
AO	50	M	1261259	378305
GBM	56	F	47727954	20927301
Astrocytoma	27	F	1721976	3137530
Astrocytoma	32	F	31887460	45294696
GBM	61	M	20320432	25663090
Astrocytoma	27	M	28661710	45244078
Astrocytoma	39	F	4356405	1093566
AA	30	M	39642469	29777748
AO	53	F	72633527	84155405
Oligodendroglioma	43	M	22556824	58044269
GBM	31	F	137027818	86226588
GBM	31	F	33629589	4564017
Astrocytoma	29	M	125998378	34281034
OA	50	M	97829567	61572655
OA	34	M	14875269	47941656

Table S2, Related to Figure 3E: Patient characteristics for samples used in GC-MS analysis of metabolites shown in Figure 3E. Abbreviations: AA; Anaplastic astrocytoma, AO; Anaplastic oligodendroglioma, AOA; Anaplastic oligoastrocytoma, AUC; area under the curve, GBM; Glioblastoma.

Supplemental Experimental Procedures

All chemicals were from Sigma (UK) unless otherwise specified**.**

Molecular cloning and cell transduction with lentiviral vectors

Human IDH2 cDNA was amplified by PCR using primers, which added 1X-FLAG tag to the 3' end of the sequence. This was cloned as ClaI-NheI fragment into the pCC.sin.36.MCS.PPTWpre.CMV.tTA-S2tet lentiviral transfer vector. Subsequently a recombinant PCR-based approach, using IDH2 cDNA as a template was applied to construct the IDH2 R172K mutant, which was cloned into the same lentiviral transfer vector as a ClaI-Nhe fragment, by substituting the IDH2 cassette with the IDH2-R172K mutant cassette. As a control, cells were transduced with a pCC.sin.36.eGFP.PPT.Wpre.CMV.tTA-s2tet, encoding eGFP and pCC.sin.36.IDH2WT.PPTWpre.CMV.tTA-S2tet, encoding the wild type sequence of human IDH2. PCR primers for the above are available upon request. Human IDH1 wild type and R132H mutant vectors, vector stocks and titration were prepared as described in (Bardella et al., 2016).

Cell culture

ON_TARGETplus pools used were: (L-012349-00 [PYCR1], L-016646-00 [PYCR2] or D-001810-10 [non-targeting]; Thermo Fisher, UK) at 25 nM using DharmaFECT 1 transfection reagent (Thermo Fisher, UK) 24 h post seeding. Cells were lysed at various time points post-transfection (see Figures for details) to evaluate knockdown.

Quantitative real-time PCR

Total RNA was extracted using the RNeasy Mini Kit (Qiagen, 74104) according to the manufacture's protocol. 1 µg RNA per sample was subjected to reverse transcription using Moloney Murine Leukemia Virus Reverse Transcriptase (MMLV-RT) kit (Promega, M1701). 10 µL of the resulting cDNA was used with TaqMan® gene expression master mix (AB, 4369016) for quantitative real-time PCR using AB 7500 Real Time PCR System. The

following primers and probes were used: *PYCR1* (Hs01048016_m1), *PYCR2* (Hs01016460_gH), *ALDH18A1* (Hs00913261_m1), *ACTIN* (Hs01060665_g1) (ThermoFisher Scientific). The expression of ALDH18A1, PYCR1 and PYCR2 were normalised to actin as housekeeping gene. Comparative analysis across samples was calculated using the $2^{-\Delta\Delta CT}$ method.

O_2 Consumption Measurements

Cells were seeded at 2 x 10^5 onto 6-well plates in standard culture conditions and were transfected 24 h later with targeting siRNA against PYCR1 and PYCR2. The cells were harvested and re-suspended in complete media. 4 x 10^5 cells in 300 µl were added to the electrode chamber and the oxygen consumption rate was measured over a 5 min period using Oxygraph software (http://www.hansatech-instruments.com/). Cells were kept in suspension using a stirring bar and the chamber temperature was maintained at 37°C through the use of a heating block. After recording for 5 min, KCN 700 µM (Sigma-Aldrich, 60178) was added to the electrode chamber to inhibit cellular respiration and the oxygen consumption was measured for a further 3 min. The final respiration rate was obtained by subtracting the oxygen consumption rate in presence of KCN to the oxygen consumption rate in the absence of KCN.

NMR Spectroscopy

4 x 10^6 cells were plated onto 15 cm dishes and cultured in standard medium overnight. Media was replaced with basic formulation DMEM supplemented with $^{13}C_6$ glucose or $^{13}C_5$ glutamine at 10 mM and 2 mM respectively for 24 h prior to extraction. At the conclusion of tracer experiments, cells were washed with ice-cold 0.9% saline solution and extracted in 1.2 mL pre-chilled methanol (-20^{o}C), water (4^{o}C) and chloroform (-20^{o}C) in a 1:1:1 ratio. Cell lysates were vortexed for 15 min at 4^{o}C and immediately centrifuged at 15,000 *g* for 15 min at 4^{o}C. Extraction was performed on three different cultures for each labelling experiment.

Dried samples were re-suspended in 60 µL of 100 mM sodium phosphate buffer (pH7.0) containing 500 µM DSS and 2 mM Imidazole, 10% D_20, pH 7.0. Samples were vortexed, sonicated (5-15 min) and centrifuged briefly, before transferred to 1.7 mm NMR tubes using an automated Gilson.One-dimensional (1D)-^{1}H-NMR spectra and two-dimensional (2D)-^{1}H,^{13}C-Heteronuclear Single Quantum Coherence Spectroscopy (HSQC) NMR spectra were acquired using a 600-MHz Bruker Avance III spectrometer (Bruker Biospin) with a TCI 1.7 mm z-PFG cryogenic probe at 300 K. Spectral widths were set to 7,812.5 and 24,155 Hz for the ^{1}H and ^{13}C dimensions, respectively. 16,384 complex data points were acquired for the 1D-spectra and 512 complex data points were acquired for the ^{1}H dimension of 2D-^{1}H,^{13}C-HSQC NMR spectra. An exponentially weighted non-uniform sampling scheme was used for the indirect dimension. Here, 30% of 8,192 complex data points (2,458) were acquired. 128 transients were recorded for the 1D-NMR spectra with a relaxation delay of 4 s, and two transients were recorded for the 2D-^{1}H,^{13}C-HSQC NMR spectra with a relaxation delay of 1.5 s. Each sample was automatically tuned, matched and then shimmed (1D-TopShim) to a DSS line width of <2 Hz before acquisition of the first spectrum. Total experiment time was ~15 min per sample for 1D-^{1}H-NMR spectra and 4.5 h per sample for 2D-^{1}H,^{13}C-HSQC NMR spectra. 1D-^{1}H-NMR spectra were processed using the MATLAB-based MetaboLab software (Ludwig and Gunther, 2011). All 1D data sets were zero-filled to 131,072 data points before Fourier Transformation. The chemical shift was calibrated by referencing the DSS signal to 0 p.p.m. 1D-spectra were manually phase corrected. Baseline correction was achieved using a spline function (Ludwig and Gunther, 2011). 1D-^{1}H-NMR spectra were exported into Bruker format for metabolite identification and concentration determination using Chenomx 7.0 (ChenomxINC). 2D-^{1}H,^{13}C-HSQC NMR spectra were reconstructed using compressed sensing in the MDDNMR and NMRpipe software (Delaglio et al., 1995; Kazimierczuk and Orekhov, 2011; Orekhov and Jaravine, 2011). The final spectrum size was 1,024 real data points for the ^{1}H dimension and 16,384 real data points for the ^{13}C dimension. Analysis was performed using MetaboLab and pyGamma software was used in multiplet simulations (Smith et al., 1994). The methyl group of lactate was used

to calibrate the chemical shift based on its assignment in the human metabolome database (Wishart et al., 2013).

GC-MS

Cell analysis - cells were seeded at 2 x 10^5 onto 6-well plates in standard culture conditions and transfected with non-targeting RNA (siNT) and siRNA targeting PYCR1 (siPYCR1) and PYCR2 (siPYCR2) at 25 nM. Media was changed to basic formulation DMEM containing either 10 mM $^{13}C_6$ glucose or 2 mM $^{13}C_5$ glutamine with the other carbon source unlabelled, for 24 h prior to extraction. At the conclusion of tracer experiments, cells were washed with 2 mL ice-cold 0.9% saline solution and quenched with 0.3 mL pre-chilled methanol (-20^{o}C). After adding an equal volume of ice-cold HPLC-grade water containing 1 µg/mL D6-glutaric acid (C/D/N Isotopes Inc), cells were collected with a cell scraper and transferred to tubes containing 0.3 mL of chloroform (-20^{o}C). The extracts were shaken at 1400 rpm for 20 min at 4^{o}C and centrifuged at 16,000 *g* for 5 min at 4^{o}C. 0.3 mL of the upper aqueous phase was collected and evaporated in GC glass vials under vacuum at -4^{o}C using a refrigerated CentriVap Concentrator (Labconco). Metabolite derivatization was performed using an Agilent autosampler. Dried polar metabolites were dissolved in 15 µl of 2% methoxyamine hydrochloride in pyridine (Thermo Fisher Scientific, 25104) at 55^{o}C, followed by an equal volume of N-tert-Butyldimethylsilyl-N-methyltrifluoroacetamide with 1% tert-butyldimethylchlorosilane after 60 minutes, and incubation for a further 90 min at 55^{o}C.

GC-MS analysis was performed using an Agilent 6890GC equipped with a 30 m DB-35MS capillary column. The GC was connected to an Agilent 5975C MS operating under electron impact ionization at 70 eV. The MS source was held at 230^{o}C and the quadrupole at 150^{o}C. The detector was operated in scan mode and 1 µL of derivatised sample was injected in splitless mode. Helium was used as a carrier gas at a flow rate of 1 mL/min. The GC oven temperature was held at 80^{o}C for 6 min and increased to 325^{o}C at a rate of 10^{o}C/min for 4

min. The run time for each sample was 59 min. Measurements in selcted ion monitoring (SIM) mode were performed as described previously (Battello et al., 2016). For determination of the mass isotopomer distributions (MIDs), spectra were corrected for natural isotope abundance. Data processing from raw spectra to MID correction and determination was performed using MetaboliteDetector software (Hiller et al., 2009).

Tumor metabolite analysis

20 mg of tumor was mixed with 400 µL of 80% methanol, homogenized in a Tissuelyser-48 (Shanghai Jingxin), and then centrifuged at 14,000 rpm for 10 min at 4°C. A 200 µL aliquot of supernatant was transferred to a screw-cap V-type glass-bottom vial and dried in a vacuum-drying apparatus at 30°C for 1 h. Methoxyamine hydrochloride was dissolved in pyridine at a concentration of 20 mg/mL; 35 µL of this solution was added to the sample, and then incubated at 70°C for 0.5 h. Derivatization was performed at 70°C for 40 min following addition of 20 µL of MTBSTFA. The sample (1 µL) was subjected to GC-MS, with a total run time of 32 min. A capillary column (HP-5ms Intuvo, 30 m × 0.25 mm × 0.25 µm; Agilent Technologies) using helium as a carrier gas was utilized for GC separation. The inlet model was splitless, and its temperature was 250°C. Parameters for GC-MS were as follows: 100°C for 3 min; ramp 10°C/min to 140°C, 8°C/min to 260°C, and 10°C/min to 310 °C; and then hold for 5 min at 310°C. The total run time was 32 min. The temperature of the injector was set at 280°C, and that of the MSD Transfer Line was 290°C. Ion source was EI (70 eV) at a temperature of 230°C. Mass scan range was from 50 to 600 m/z.

Redox measurements

Cells were seeded at 2 x 10^4 onto 8-well chamber slides (Thistle Scientific, IB-80826) for NAD(P)H autofluorescence measurements, or 6 x 10^3 in 96-well plates for NAD:NADH

assay. Both were transfected 24 h later with targeting and non-targeting siRNA against PYCR1 or PYCR2 where shown before NAD(P)H imaging or biochemical analysis 48 h later. NAD(P)H was excited at λ = 351/364 nm using the argon UV laser module on a Zeiss UV Axiovert confocal autofluorescence, and autofluorescence captured at λ = 385-470 nm using a photomultiplier tube (PMT) (1024 x 1024 pixels; 12-bit). Carbonyl cyanine m-chlorophenyl hydrazine (CCCP) 20 µM (Sigma-Aldrich, C2759) and Rotenone 60 µM (Sigma-Aldrich, R8875) were added to each well to achieve basal and maximal NAD(P)H autofluorescence, respectively. User-blinded offline analysis was performed using Fiji software (http://fiji.sc/) and 48-126 random visual fields were analyzed per experimental condition. Images presented were exported into ImageJ, and noise reduction performed using the 'remove outliers' function with standard settings. NAD:NADH assay (NAD/NADH Glo^{TM} Assay (Promega, G9071) was performed as per manufacturer's protocol.

ROS measurements

Cells were seeded at 2 x 10^5 onto 6-well plates in standard culture conditions and as described above. To assay for ROS, media was replaced with HBSS before incubation with 5 µM of MitoSOX Red (Thermofisher, M36008) at 37°C for 10 minutes. The cells were trypsinized and subsequently collected in HBSS with 1% FBS. Using an LSRFortessa X-20 flow cytometer, fluorescence at 575nm was measured and mean fluorescence intensity of 10,000 events in triplicate assessed using FloJo software.

SRB assay

Cells were treated with 50 nM rotenone for 72 h prior to being fixed in 20% (v/v) ice-cold trichloroacetic acid solution (TCA) (Sigma-Aldrich, T0699) for 30 min at 4^{o}C. Plate wells were washed with water and once dry, intracellular protein was stained using 0.4% (w/v)

sulfohodamine B (SRB) (Sigma-Aldrich, 230162) in 1% acetic acid for 10 min at room temperature. After washing with 1% acetic acid to reduce non-specific staining, SRB was dissolved in 50 mM Tris/HCl pH 8.8 once dry. 100 µL/well was aliquoted for quantification by absorbance at 495 nm on FLUOstar Omega (BMG LabTech). Final sample absorbance values were determined by calculating the mean blank-corrected absorbance for each replicate, where 50 mM Tris/HCl pH 8.8 alone was used as the blank.

References

Bardella, C., Al-Dalahmah, O., Krell, D., Brazauskas, P., Al-Qahtani, K., Tomkova, M., Adam, J., Serres, S., Lockstone, H., Freeman-Mills, L*., et al.* (2016). Expression of Idh1(R132H) in the Murine Subventricular Zone Stem Cell Niche Recapitulates Features of Early Gliomagenesis. Cancer Cell *30*, 578-594.

Battello, N., Zimmer, A.D., Goebel, C., Dong, X., Behrmann, I., Haan, C., Hiller, K., and Wegner, A. (2016). The role of HIF-1 in oncostatin M-dependent metabolic reprogramming of hepatic cells. Cancer Metab *4*, 3.

Delaglio, F., Grzesiek, S., Vuister, G.W., Zhu, G., Pfeifer, J., and Bax, A. (1995). NMRPipe: a multidimensional spectral processing system based on UNIX pipes. J Biomol NMR *6*, 277-293.

Hiller, K., Hangebrauk, J., Jager, C., Spura, J., Schreiber, K., and Schomburg, D. (2009). MetaboliteDetector: comprehensive analysis tool for targeted and nontargeted GC/MS based metabolome analysis. Anal Chem *81*, 3429-3439.

Kazimierczuk, K., and Orekhov, V.Y. (2011). Accelerated NMR spectroscopy by using compressed sensing. Angew Chem Int Ed Engl *50*, 5556-5559.

Ludwig, C., and Gunther, U.L. (2011). MetaboLab--advanced NMR data processing and analysis for metabolomics. BMC Bioinformatics *12*, 366.

Orekhov, V.Y., and Jaravine, V.A. (2011). Analysis of non-uniformly sampled spectra with multi-dimensional decomposition. Prog Nucl Magn Reson Spectrosc *59*, 271-292.

Smith, S.A., Levante, T.O., Meier, B.H., and Ernst, R.R. (1994). Computer-Simulations in Magnetic-Resonance - an Object-Oriented Programming Approach. J Magn Reson Ser A *106*, 75-105.

Wishart, D.S., Jewison, T., Guo, A.C., Wilson, M., Knox, C., Liu, Y., Djoumbou, Y., Mandal, R., Aziat, F., Dong, E*., et al.* (2013). HMDB 3.0--The Human Metabolome Database in 2013. Nucleic Acids Res *41*, D801-807.